

Entangling a Hole Spin with a Time-Bin Photon: A Waveguide Approach for Quantum Dot Sources of Multi-Photon Entanglement

Martin Hayhurst Appel,¹ Alexey Tiranov,¹ Simon Pabst,¹ Ming Lai Chan,¹ Christian Starup,¹ Ying Wang,¹ Leonardo Midolo,¹ Konstantin Tiurev,¹ Sven Scholz,² Andreas D. Wieck,² Arne Ludwig,² Anders Søndberg Sørensen,¹ and Peter Lodahl¹

¹*Center for Hybrid Quantum Networks (Hy-Q), The Niels Bohr*

Institute, University of Copenhagen, DK-2100 Copenhagen Ø, Denmark

²*Lehrstuhl für Angewandte Festkörperphysik, Ruhr-Universität Bochum, Universitätsstraße 150, 44801 Bochum, Germany*

(Dated: June 10, 2022)

Deterministic sources of multi-photon entanglement are highly attractive for quantum information processing but are challenging to realize experimentally. In this paper, we demonstrate a route towards a scalable source of time-bin encoded Greenberger-Horne-Zeilinger and linear cluster states from a solid-state quantum dot embedded in a nanophotonic crystal waveguide. By utilizing a self-stabilizing double-pass interferometer, we measure a spin-photon Bell state with $(67.8 \pm 0.4)\%$ fidelity and devise steps for significant further improvements. By employing strict resonant excitation, we demonstrate a photon indistinguishability of $(95.7 \pm 0.8)\%$, which is conducive to fusion of multiple cluster states for scaling up the technology and producing more general graph states.

A near-deterministic source of multi-photon entanglement will enable significant advancements in quantum information processing such as one-way quantum computing consuming few-photon Greenberger-Horne-Zeilinger (GHZ) states [1, 2] or one-way photonic repeaters relying on large photonic graph states [3, 4]. Until now, spontaneous parametric down-conversion has been the leading source of entangled photons and has enabled demonstrations of 12 entangled photons [5]. However, this approach is based on probabilistic photon sources and is thus challenging to scale up. An alternative approach proposed by Lindner and Rudolph exploits a single solid-state quantum emitter as an on-demand entanglement source [6]. In their proposal, a semiconductor quantum dot (QD) containing a single spin is repeatedly excited to create a linear cluster state of polarization encoded photons. Despite its elegance, this approach has several experimental drawbacks. Specifically, natural spin precession is employed in a weak external magnetic field for which the QD spin is poorly decoupled from the nuclear spin bath [7–9]. Additionally, the need to collect two orthogonally polarized modes is often experimentally incompatible with the resonant excitation required for high photon indistinguishability [10]. These challenges were partly combated in the landmark experiment of Ref. [11], where the use of dark-exciton states and non-resonant excitation enabled the explicit demonstration of three-qubit entanglement and extrapolation to five qubits. Nonetheless, the further scalability of multi-photon entanglement sources has been an open question so far only addressed theoretically [12, 13]. A key feature is the generation of high-fidelity multi-photon entanglement while preserving photon indistinguishability; a crucial requirement for fusion-based photonic quantum computing [1, 14].

In this paper, we perform the first demonstration of QD spin-photon entanglement using a time-bin protocol

capable of generating multi-photon GHZ and linear cluster states. This protocol has been used to demonstrate spin-photon entanglement from nitrogen-vacancy centers [15–17], the first steps using a micropillar QD source were implemented in Ref. [18] without proving entanglement, and a detailed theoretical treatment was recently published [12, 13]. Contrary to the Lindner–Rudolph protocol, we apply strong magnetic fields which permit the use of spin-echo pulses and render the protocol insensitive to spin-dephasing [12]. Additionally, a single optical transition is excited resonantly and emits highly indistinguishable photons into a single-mode photonic crystal waveguide (PCW) with near-unity internal collection efficiency [19, 20]. Here, we focus on measuring spin-photon Bell states using a novel double-pass interferometer and determine a fidelity of 67.8%. This fidelity is predominantly limited by the quality of the spin rotations, which can be substantially improved in future experiments [21].

The entanglement protocol builds upon our recent work on uniting optical cycling transitions with optical spin control [22] as summarised in FIG. 1a. A positively charged InAs QD in an in-plane (Voigt geometry) magnetic field $B_y = 2\text{T}$ gives rise to a pair of Zeeman-split heavy-hole ground states $|\uparrow\rangle$ and $|\downarrow\rangle$, which are used as a spin qubit [23], and a pair of Zeeman-split trions $|\uparrow\uparrow\downarrow\rangle$ and $|\downarrow\downarrow\uparrow\rangle$ enabling photon generation. The four linear dipoles are driven by a red-detuned Raman laser to rotate the spin qubit [21, 22] while the PCW (FIG. 1b) selectively enhances the optical transitions resulting in the optical cyclicity $C = \gamma_y/\gamma_x = 14.7 \pm 0.2$ [22], which is otherwise unity in a homogeneous environment or a cylindrically symmetric cavity. Spin-photon entanglement is then generated according to the protocol in FIG. 1c. Optical pumping

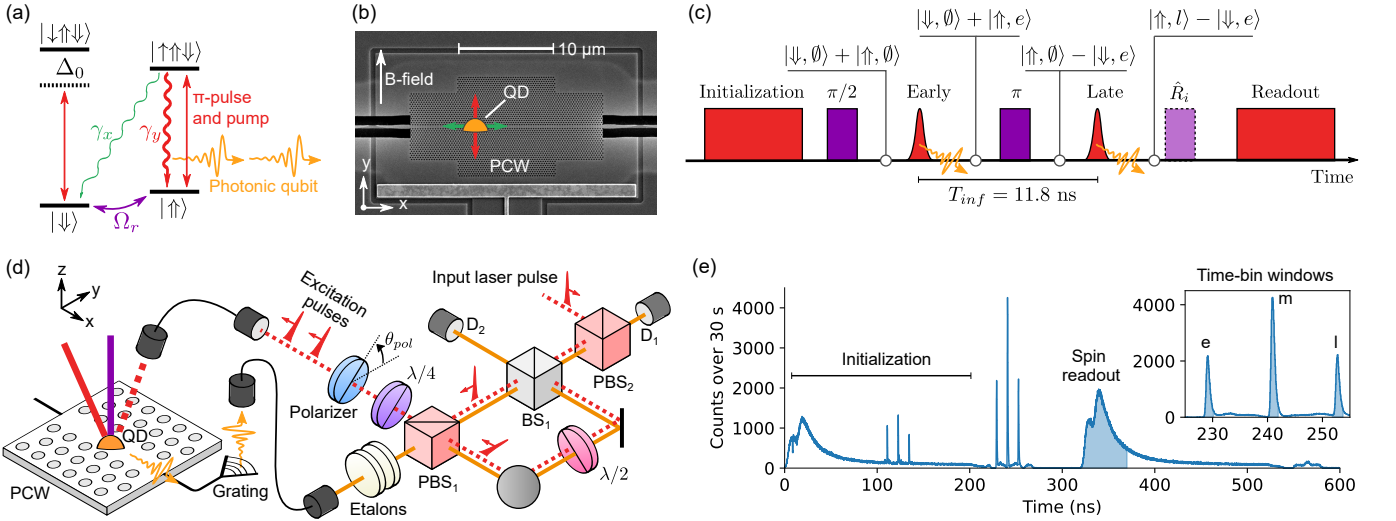


FIG. 1. (color online) Time-bin entanglement protocol. **(a)** Energy level diagram of a positively charged QD in a Voigt magnetic field. The $|\uparrow\rangle \leftrightarrow |\uparrow\uparrow\downarrow\rangle$ transition is used to emit photonic qubits and to perform spin initialization and readout via optical pumping. The trion decay paths have rates γ_y and γ_x , Ω_r is the spin Rabi frequency and Δ_0 is the sum of the Zeeman splittings. **(b)** Scanning electron micrograph of the PCW with QD dipoles overlaid. **(c)** Experimental pulse sequence consisting of pumping pulses (red squares), rotation pulses (purple squares) and fast optical π -pulses (red pulses). The spin-photon state is indicated on top with $|\emptyset\rangle$ denoting photon vacuum and $|e\rangle$ ($|l\rangle$) denoting an early(late) photon. **(d)** Experimental setup. The PCW embedded QD is subjected to lasers propagating from free space. A double-pass TBI defines the excitation pulses (dashed red line) and interferes the emitted photons (solid orange line) resulting in mutual phase stability. A polariser with angle θ_{pol} determines the photonic readout basis. $\lambda/2$ ($\lambda/4$) denotes half(quarter)-waveplates. **(e)** Fluorescence histogram resulting from Bell state generation summed over both detectors including a 50 ns spin readout detection window (shaded area). The inset shows a magnified view of the early(e), middle(m), and late(l) detection windows (2 ns each) which herald the measurement basis of the photonic qubit. The peaks at 120 ns are optical reflections inside the TBI.

initializes $|\downarrow\rangle$ and a $\hat{R}_y(\pi/2)$ rotation around the y-axis prepares the superposition state $(|\downarrow\rangle + |\uparrow\rangle)/\sqrt{2}$. The QD is then subjected to a y-polarised optical π -pulse resonant with $|\uparrow\rangle \leftrightarrow |\uparrow\uparrow\downarrow\rangle$. As the other y-polarised transition is detuned by $\Delta_0 = 2\pi \times 17$ GHz, trion excitation and thus photon emission is conditioned on $|\uparrow\rangle$. The enhanced cyclicity ensures photon emission via the spin-preserving $|\uparrow\uparrow\downarrow\rangle \rightarrow |\uparrow\rangle$ transition with probability $C/(C+1) \approx 94\%$. Thus, an early excitation entangles $|\uparrow\rangle$ with an early photon $|e\rangle$. The spin states are then swapped by a π -rotation before applying a late excitation pulse resulting in the emission of a late photon $|l\rangle$. The resulting state is the spin-photon Bell state

$$|\psi_{Bell}\rangle = (e^{i\phi_e} |\uparrow, l\rangle - |\downarrow, e\rangle)/\sqrt{2}, \quad (1)$$

where the emission time of the single photon is maximally entangled with the hole spin, and ϕ_e is the phase difference between the two excitation pulses. By working in the rotating frame of the Raman laser, the spin does not precess and only rotates when we actively apply a Raman pulse in contrast to Refs. [6, 11].

The entangled state is generated and analyzed using the setup in FIG. 1d. The QD is held at 4 K in a closed cycle cryostat and is subjected to lasers propagating from free space. The early and late excitation

pulses are generated by injecting a single pulse into the excitation-pass (dashed line in FIG. 1d) of a time-bin interferometer (TBI) which sets the phase ϕ_e and the time delay $T_{inf} = 11.8$ ns between the early and late pulses. T_{inf} is sufficient for performing photon emission (400 ps lifetime) and a π -rotations (7 ns). The QD emits photons into the guided PCW mode, which is coupled to a single-mode fiber via a grating coupler [24]. From here the photon stream enters the detection-pass of the TBI (orange line in FIG. 1d) where a pair of 3 GHz FWHM etalon filters are used to reject the Raman laser scatter and the QD phonon sideband [25]. Next, a polarising beamsplitter PBS₁ transmits or reflects with equal probability. This passive routing leads to three detection windows (see FIG. 1e) which herald the photonic measurement basis. An early(late) detection corresponds to an early(late) photon propagating through the short(long) TBI arm and thus constitutes a Z-basis measurement. By contrast, the middle window represents the time-bin photon interfering with itself on BS₁. A photon click on detector D₁ or D₂ thus projects the photon onto $|\phi^\pm\rangle = (|e\rangle \pm e^{i\phi_d} |l\rangle)/\sqrt{2}$ where ϕ_d is the phase of the detection-pass. Since excitation and detection-passes use the same interferometer the phases ϕ_d and ϕ_e are mutually stable [26] giving a stable detection pattern without the need for active stabilization [16, 27].

We now proceed to quantify the spin-photon entanglement using the approach of Ref. [28] which is scalable to future, large N -qubit GHZ states by only requiring $N + 1$ measurement settings for an exact fidelity estimate. Adapting the technique to a Bell state gives

$$\mathcal{F}_{Bell} = \frac{\langle \hat{P}_z \rangle}{2} + \frac{\langle \hat{M}_y \rangle - \langle \hat{M}_x \rangle}{4}, \quad (2)$$

where $\hat{P}_z = |\uparrow\rangle\langle\uparrow| + |\downarrow\rangle\langle\downarrow|$ measures the classical correlations and $\hat{M}_x = \hat{\sigma}_x^{(s)} \otimes \hat{\sigma}_x^{(p)}$ and $\hat{M}_y = \hat{\sigma}_y^{(s)} \otimes \hat{\sigma}_y^{(p)}$ measure both qubits along X and Y, respectively. $\hat{\sigma}$ denotes single qubit Pauli matrices, s(p) superscripts denote spin(photonic) qubit, and we designate the logical qubits $|0\rangle = |\uparrow\rangle, |1\rangle = |\downarrow\rangle$ and $|e\rangle = |\uparrow\rangle, |l\rangle = |\downarrow\rangle$. We post-select on measuring photons in both the photonic and spin readout windows and achieve a 124 Hz coincidence rate when repeating the experiment at a 1.65 MHz repetition rate. As the spin readout can only detect $|\uparrow\rangle$ we apply a \hat{R}_i rotation prior to readout (FIG. 1c) fulfilling $\hat{R}_i|s\rangle = |\uparrow\rangle$ to realize the desired spin projector $|s\rangle\langle s|$. FIG. 2a shows the results of a ZZ-basis measurement. Projection on $|e\rangle$ and $|l\rangle$ is given by the photon detection time (both detectors are treated equally) and the \hat{R}_i pulse is toggled between a 0 and a π rotation to realize projections onto $|\uparrow\rangle$ and $|\downarrow\rangle$, respectively. Normalizing across all four projections yields $\langle \hat{P}_z \rangle = (89.3 \pm 0.4)\%$. The imbalance of $|\uparrow\rangle|l\rangle$ and $|\downarrow\rangle|e\rangle$ is primarily a consequence of the imperfect \hat{R}_i spin rotation (discussed later) which reduces the probability of measuring $|\downarrow\rangle$.

In order to measure time-bin encoded photons in the equatorial plane of the Bloch sphere, we add a controllable phase difference between the early and late excitation pulses: The pulses are combined on PBS₁ (FIG. 1d), converted to opposite circular polarizations with a $\lambda/4$ plate, and projected onto the transmission axis of a rotatable polarizer, which adds $2\theta_{pol}$ to the phase ϕ_e . The effect of θ_{pol} is evident from the gray data in FIG. 2b where classical excitation pulses are reinjected into the detection-pass. This reveals a full oscillation in the detector contrast with near-perfect visibility. The angle $\theta_{pol} = \theta_0$ gives bunching on detector D₁ and corresponds to the condition $\phi_d = \phi_e$. θ_0 depends on the specific TBI alignment but is stable on a week-long timescale. We then run the entanglement protocol, project the QD spin onto $|\pm X\rangle_s = (|\uparrow\rangle \pm |\downarrow\rangle)/\sqrt{2}$ (for $\hat{R}_i = \hat{R}_y(\pm\pi/2)$) and measure the spin state dependent contrast, see FIG. 2b. Crucially, the two fringes are perfectly in-phase and out-of-phase with the classical TBI response. In summary, measuring the photon in the X-basis corresponds to setting $\theta_{pol} = \theta_0$ and assigning the photon states $|+X\rangle_p$ and $|-X\rangle_p$ to a middle window detection on D₁ and D₂, respectively. FIG. 2c shows the outcomes of an XX-basis measurement. The outcomes are normalized as before and the contrast between the positive and negative eigenstates of \hat{M}_x results

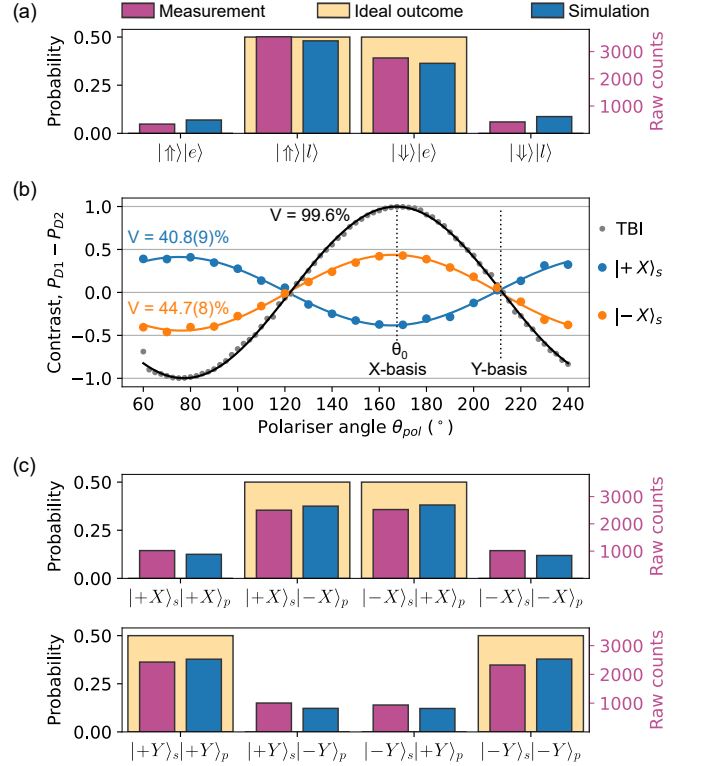


FIG. 2. (color online) Entanglement verification. **(a)** Spin-photon Bell state measured in ZZ-basis. Magenta bars denote the measured spin-photon coincidences during a 120 s acquisition. The right y-axis indicates raw counts and the left y-axis shows the probability normalized across all four outcomes. The yellow and blue bars represent the ideal and simulated detection patterns, respectively. **(b)** Determination of the photonic readout basis. The y-axis indicates the normalized intensity difference between the two TBI detectors in the middle window. The gray dots show the TBI response to a classical input while the blue and orange curves denote spin-photon coincidences when projecting the spin on $|\pm X\rangle_s$ (legend). The fits follow $V \cos(2(\theta_{pol} - \theta_0))$. Error bars are within the data points. **(c)** Spin-photon measurements in the XX-basis (top row) and YY-basis (bottom row). The s and p subscripts denote spin and photonic qubit, respectively. Axes and legends follow (a).

in $\langle \hat{M}_x \rangle = (-42.3 \pm 1.1)\%$. The \hat{M}_y measurement is similarly realized by setting $\theta_{pol} = \theta_0 + \pi/4$ and $\hat{R}_i = \hat{R}_x(\pm\pi/2)$ leading to $\langle \hat{M}_y \rangle = (42.1 \pm 1.1)\%$. By applying Eq. (2) we arrive at the final estimate $\mathcal{F}_{Bell}^{raw} = (65.7 \pm 0.4)\%$ which exceeds the classical threshold of 50% by 39 standard deviations using only 6 minutes of acquisition and no corrections. We note that some of the recorded spin-photon coincidences are due to uncorrelated laser leakage. However, this contribution is minor and correcting for the background (as in Ref. [17]) leads to a corrected fidelity of $\mathcal{F}_{Bell}^{corr} = (67.8 \pm 0.4)\%$. NV centers [16, 17] have produced similar quality Bell states but with greater reliance on background subtraction. In the interest of understanding the relevant error

mechanisms we perform a Monte Carlo simulation of the experiment including all errors and backgrounds (Supplementary Material [29]). This yields the fidelity $\mathcal{F}_{Bell}^{sim} = 67.8\%$ (to be compared against \mathcal{F}_{Bell}^{raw}) and the detection pattern in FIG. 2 which is in good agreement with the experimental values and supports our error analysis.

We now highlight two of the errors limiting \mathcal{F}_{Bell} . The dominant error is the quality of Raman pulses used for X and Y rotations of the hole spin. By measuring the dampening of Rabi oscillations between $|\uparrow\rangle$ and $|\downarrow\rangle$ we extract a π -pulse fidelity of $F_\pi = 88.5\%$ which is predominantly limited by incoherent spin-flips between the two spin states (Supplementary Material [29]). Naturally, the time-bin protocol relies on highly coherent spin control, and $F_\pi = 88.5\%$ alone limits the Bell state fidelity to 77% according to Monte Carlo simulations. Thus, we may attribute $\sim 70\%$ of the measured infidelity to this mechanism. Fortunately, a recent scheme using electron spins and nuclear spin cooling [21] demonstrated $F_\pi = 98.8\%$ and could readily be implemented in the experimental protocol. This would increase the achievable fidelity to $\mathcal{F}_{Bell} = 97.3\%$ (neglecting other errors).

A second relevant error is the single-photon purity and indistinguishability of the emitted photons. The latter error reduces the measurement contrast in the XX and YY bases [12] and is additionally relevant for combining multiple smaller cluster states through entanglement fusion [2]. To accurately characterize the time-bin encoded photon, we retain the magnetic field and minimally modify the pulse sequence to emit two separable single photons (FIG. 3a). By using the TBI, we simultaneously measure the $g^{(2)}$ intensity autocorrelation and Hong–Ou–Mandel (HOM) visibility by letting the detection time herald the experiment. FIG. 3b shows the delays between photons recorded in either the early or late detection windows and constitutes two sets of $g^{(2)}$ measurements. A slight bunching is observed for short delays owing to non-deterministic initialization of the hole charge state. Normalizing $g^{(2)}$ at long delays and averaging over early and late gives $g^{(2)}(0) = (4.7 \pm 0.6)\%$ from which 1.1% may be attributed to excitation laser scatter. The remaining contribution is likely a result of multi-photon emission owing to the fast, Purcell enhanced decay rate $\gamma_0 = (\gamma_x + \gamma_y) = 2.54 \text{ ns}^{-1}$ and the FWHM duration of the π -pulse $T_{opt} = 35 \text{ ps}$. T_{opt} represents a trade-off [12, 13] between multi-photon emission (minimized for $T_{opt} \ll \gamma_0^{-1}$) and unwanted excitation of $|\downarrow\rangle \leftrightarrow |\downarrow\uparrow\downarrow\rangle$ (minimized for $T_{opt} \gg \Delta_0^{-1}$). A larger magnetic field will increase Δ_0 and permit a shorter T_{opt} and thus reduced $g^{(2)}(0)$. FIG. 3c shows the delay between two photons recorded within the same experimental repetition when at least one photon was measured in the middle window. Following

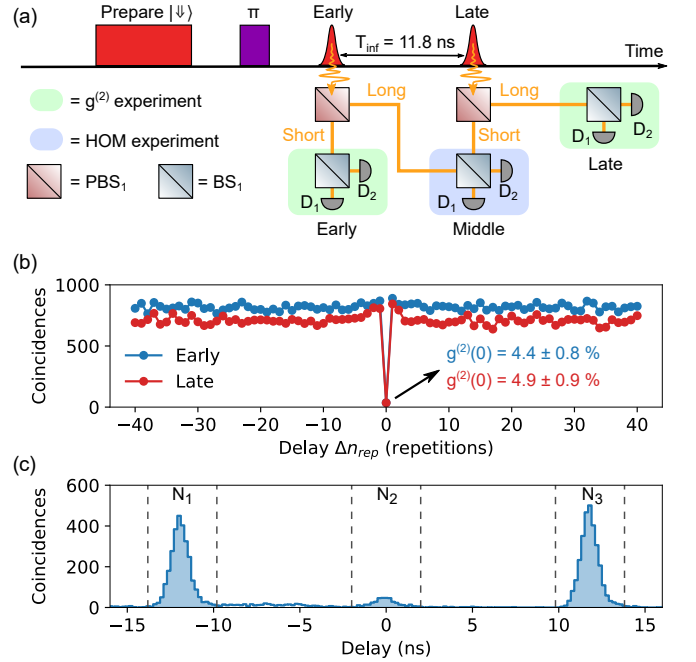


FIG. 3. (color online) Single-photon characterization. (a) Pulse sequence for $g^{(2)}$ and HOM measurements. A pump and a Raman pulse prepare $|\downarrow\downarrow\rangle$ and optical π -pulses are used to emit two photons. The TBI (here in a path-representation) can either measure a single photon on a BS ($g^{(2)}$ measurement) or interfere two photons on a BS (HOM measurement). Waveplates (not shown) ensure identical polarization at the middle detection. (b) $g^{(2)}$ measurement results. The x-axis indicates the delay between photons in units of the experimental repetition time. (c) Photon coincidences within the same experimental repetition yielding a HOM measurement.

Ref. [30], this estimates a raw indistinguishability of $\mathcal{V}^{raw} = 1 - 2N_2/(N_1 + N_3) = (86.5 \pm 0.6)\%$ (integration windows given in FIG. 3c). \mathcal{V}^{raw} is primarily limited by the finite $g^{(2)}(0)$ according to $\mathcal{V}^{raw} \approx \mathcal{V}/(1 + 2g^{(2)}(0))$, which assumes the multi-photon contribution to consist of distinguishable photons [30, 31]. Correcting for $g^{(2)}(0)$ and the slight imperfection of the TBI yields a corrected HOM visibility of $\mathcal{V} = (95.7 \pm 0.8)\%$ which is compatible with the QD state of the art [32–34].

In summary, we have used a PCW embedded QD to implement a scalable protocol for the generation of time-bin entangled photonic states. This is facilitated by the PCW platform which offers a compelling marriage of spin control and photonic enhancement. Operating at high magnetic fields allows spin initialization without projective measurements and the photon indistinguishability is independent of the magnetic field strength as a single optical transition is used for emission. Our insights from theory and simulation show a clear path towards improving the fidelity with the quality of spin rotations requiring the most attention. Indeed, given

realistic PCW parameters and perfect Raman pulses we expect to reach an error level of 2.1% per emitted photon [13]. The generalization to more photons is straightforward and only requires additional rotation and excitation pulses to create a multi-photon GHZ or 1D-cluster state with photonic qubits emitted every 28 ns. We have attempted a three-qubit GHZ state (Supplementary Material [29]) but only measured a $\mathcal{F}_{GHZ} = (42.3 \pm 1.4)\%$ fidelity due to the imperfect Raman pulses.

Another promising aspect of our approach is the entanglement generation rate. Our 124 Hz Bell-state detection rate is already favourable against similar protocols based on NV centers (7 mHz in Ref. [17]) despite our limited and non-optimized total detection efficiency $\eta_{total} = 0.3\%$. Indeed, a QD-to-fiber collection efficiency of $\eta = 7\%$ was recently demonstrated in a similar PCW structure and further realistic improvements may facilitate collection efficiencies as high as $\eta = 78\%$ [34]. Finally, we note that the high magnetic field regime can give access to nuclear magnon modes [35], which may be used as a long-lived quantum memory for repeater applications [36] or as an ancillary qubit for use in photonic graph state generation [37, 38].

The supporting data for this Letter are openly available from [52].

The authors thank Alisa Javadi, Matthias C. Löbl and Richard J. Warburton for valuable discussions. We gratefully acknowledge financial support from Danmarks Grundforskningsfond (DNRF 139, Hy-Q Center for Hybrid Quantum Networks), Styrelsen for Forskning og Innovation (FI) (5072-00016B QUANTECH), the European Union's Horizon 2020 research and innovation programme under grant agreement No. 820445 (project name Quantum Internet Alliance), the European Union's Horizon 2020 Research and Innovation programme under grant agreement No. 861097 (project name QUDOT-TECH). S. S., A. D. W., and A. L. gratefully acknowledge financial support from Deutsche Forschungsgemeinschaft (DFG) (TRR 160 and LU2051/1-1), the BMBF through project QR.X grant No. 16KISQ009 and the DFH/UFA through grant No. CDFA-05-06.

[1] M. Gimeno-Segovia, P. Shadbolt, D. E. Browne, and T. Rudolph, From Three-Photon Greenberger-Horne-Zeilinger States to Ballistic Universal Quantum Computation, *Phys. Rev. Lett.* **115**, 020502 (2015).
 [2] T. Rudolph, Why i am optimistic about the silicon-photonic route to quantum computing, *APL Photonics* **2**, 030901 (2017).
 [3] J. Borregaard, H. Pichler, T. Schröder, M. D. Lukin, P. Lodahl, and A. S. Sørensen, One-way quantum repeater based on near-deterministic photon-emitter interfaces, *Phys. Rev. X* **10**, 021071 (2020).

[4] K. Azuma, K. Tamaki, and H.-K. Lo, All-photonic quantum repeaters, *Nat. Commun.* **6**, 6787 (2015).
 [5] H. S. Zhong, Y. Li, W. Li, L. C. Peng, Z. E. Su, Y. Hu, Y. M. He, X. Ding, W. Zhang, H. Li, L. Zhang, Z. Wang, L. You, X. L. Wang, X. Jiang, L. Li, Y. A. Chen, N. L. Liu, C. Y. Lu, and J. W. Pan, 12-Photon Entanglement and Scalable Scattershot Boson Sampling with Optimal Entangled-Photon Pairs from Parametric Down-Conversion, *Phys. Rev. Lett.* **121**, 250505 (2018).
 [6] N. H. Lindner and T. Rudolph, Proposal for pulsed On-demand sources of photonic cluster state strings, *Phys. Rev. Lett.* **103**, 113602 (2009).
 [7] R. Stockill, C. Le Gall, C. Matthiesen, L. Huthmacher, E. Clarke, M. Hugues, and M. Atatüre, Quantum dot spin coherence governed by a strained nuclear environment, *Nat. Commun.* **7**, 1 (2016).
 [8] J. H. Prechtel, A. V. Kuhlmann, J. Houel, A. Ludwig, S. R. Valentin, A. D. Wieck, and R. J. Warburton, Decoupling a hole spin qubit from the nuclear spins, *Nat. Mater.* **15**, 981 (2016).
 [9] L. Huthmacher, R. Stockill, E. Clarke, M. Hugues, C. LeGall, and M. Atatüre, Coherence of a dynamically decoupled quantum-dot hole spin, *Phys. Rev. B* **97**, 241413(R) (2018).
 [10] Y. M. He, Y. He, Y. J. Wei, D. Wu, M. Atatüre, C. Schneider, S. Höfling, M. Kamp, C. Y. Lu, and J. W. Pan, On-demand semiconductor single-photon source with near-unity indistinguishability, *Nat. Nanotechnol.* **8**, 213 (2013).
 [11] I. Schwartz, D. Cogan, E. R. Schmidgall, Y. Don, L. Gantz, O. Kenneth, N. H. Lindner, and D. Gershoni, Deterministic generation of a cluster state of entangled photons., *Science* **354**, 434 (2016).
 [12] K. Tiurev, P. L. Mirambell, M. B. Lauritzen, M. H. Appel, A. Tiranov, P. Lodahl, and A. S. Sørensen, Fidelity of time-bin entangled multi-photon states from a quantum emitter, *Phys. Rev. A* **104**, 052604 (2021).
 [13] K. Tiurev, M. H. Appel, P. L. Mirambell, M. B. Lauritzen, A. Tiranov, P. Lodahl, and A. S. Sørensen, High-fidelity multiphoton-entangled cluster state with solid-state quantum emitters in photonic nanostructures, *Phys. Rev. A* **105**, L030601 (2022).
 [14] R. Uppu, L. Midolo, X. Zhou, J. Carolan, and P. Lodahl, Quantum-dot-based deterministic photon-emitter interfaces for scalable photonic quantum technology, *Nat. Nanotechnol.* **16**, 1308 (2021).
 [15] B. Hensen, H. Bernien, A. E. Dreaú, A. Reiserer, N. Kalb, M. S. Blok, J. Ruitenber, R. F. Vermeulen, R. N. Schouten, C. Abellán, W. Amaya, V. Pruneri, M. W. Mitchell, M. Markham, D. J. Twitchen, D. Elkouss, S. Wehner, T. H. Taminiau, and R. Hanson, Loophole-free Bell inequality violation using electron spins separated by 1.3 kilometres, *Nature* **526**, 682 (2015).
 [16] A. Tchebotareva, S. L. Hermans, P. C. Humphreys, D. Voigt, P. J. Harmsma, L. K. Cheng, A. L. Verlaan, N. Dijkhuizen, W. De Jong, A. Dreaú, and R. Hanson, Entanglement between a Diamond Spin Qubit and a Photonic Time-Bin Qubit at Telecom Wavelength, *Phys. Rev. Lett.* **123**, 063601 (2019).
 [17] R. Vasconcelos, S. Reisenbauer, C. Salter, G. Wachter, D. Wirtitsch, J. Schmiedmayer, P. Walther, and M. Trupke, Scalable spin-photon entanglement by time-to-polarization conversion, *npj Quantum Inf.* **6**, 9 (2020).
 [18] J. P. Lee, B. Villa, A. J. Bennett, R. M. Stevenson,

- D. J. P. Ellis, I. Farrer, D. A. Ritchie, and A. J. Shields, A quantum dot as a source of time-bin entangled A quantum dot as a source of time-bin entangled multi-photon states, *Quantum Sci. Technol* **4**, 025011 (2019).
- [19] M. Arcari, I. Söllner, A. Javadi, S. Lindskov Hansen, S. Mahmoodian, J. Liu, H. Thyrrestrup, E. H. Lee, J. D. Song, S. Stobbe, and P. Lodahl, Near-Unity Coupling Efficiency of a Quantum Emitter to a Photonic Crystal Waveguide, *Phys. Rev. Lett.* **113**, 093603 (2014).
- [20] P. Lodahl, S. Mahmoodian, and S. Stobbe, Interfacing single photons and single quantum dots with photonic nanostructures, *Rev. Mod. Phys.* **87**, 347 (2015).
- [21] J. H. Bodey, R. Stockill, E. V. Denning, D. A. Gangloff, G. Éthier-Majcher, D. M. Jackson, E. Clarke, M. Hugues, C. L. Gall, and M. Atatüre, Optical spin locking of a solid-state qubit, *npj Quantum Inf.* **5**, 95 (2019).
- [22] M. H. Appel, A. Tiranov, A. Javadi, M. C. Löbl, Y. Wang, S. Scholz, A. D. Wieck, A. Ludwig, R. J. Warburton, and P. Lodahl, Coherent Spin-Photon Interface with Waveguide Induced Cycling Transitions, *Phys. Rev. Lett.* **126**, 013602 (2021).
- [23] R. J. Warburton, Single spins in self-assembled quantum dots, *Nat. Mater.* **12**, 483 (2013).
- [24] X. Zhou, I. Kulkova, T. Lund-Hansen, S. L. Hansen, P. Lodahl, and L. Midolo, High-efficiency shallow-etched grating on GaAs membranes for quantum photonic applications, *Appl. Phys. Lett.* **113**, 251103 (2018).
- [25] G. Kiršanske, H. Thyrrestrup, R. S. Daveau, C. L. Dreeßen, T. Pregolato, L. Midolo, P. Tighineanu, A. Javadi, S. Stobbe, R. Schott, A. Ludwig, A. D. Wieck, S. I. Park, J. D. Song, A. V. Kuhlmann, I. Söllner, M. C. Löbl, R. J. Warburton, and P. Lodahl, Indistinguishable and efficient single photons from a quantum dot in a planar nanobeam waveguide, *Phys. Rev. B* **96**, 165306 (2017).
- [26] H. Jayakumar, A. Predojević, T. Kauten, T. Huber, G. S. Solomon, and G. Weihs, Time-bin entangled photons from a quantum dot, *Nat. Commun.* **5**, 4251 (2014).
- [27] F. Vedovato, C. Agnesi, M. Tomasin, M. Avesani, J. Å. Larsson, G. Vallone, and P. Villoresi, Postselection-Loophole-Free Bell Violation with Genuine Time-Bin Entanglement, *Phys. Rev. Lett.* **121**, 190401 (2018).
- [28] O. Gühne, C. Y. Lu, W. B. Gao, and J. W. Pan, Toolbox for entanglement detection and fidelity estimation, *Phys. Rev. A* **76**, 030305(R) (2007).
- [29] See supplementary information at [INSERT URL] which contains additional details on experimental setup, spin control, simulations and entanglement characterisation. This also includes Refs. [39–51].
- [30] C. Santori, D. Fattal, J. Vučković, G. S. Solomon, and Y. Yamamoto, Indistinguishable photons from a single-photon device, *Nature* **419**, 594 (2002).
- [31] H. Ollivier, S. E. Thomas, S. C. Wein, I. Maillette de Buy Wenniger, N. Coste, J. C. Loredó, N. Somaschi, A. Harouri, A. Lemaitre, I. Sagnes, L. Lanco, C. Simon, C. Anton, O. Krebs, and P. Senellart, Hong-Ou-Mandel Interference with Imperfect Single Photon Sources, *Phys. Rev. Lett.* **126**, 063602 (2021).
- [32] X. Ding, Y. He, Z. C. Duan, N. Gregersen, M. C. Chen, S. Unsleber, S. Maier, C. Schneider, M. Kamp, S. Höfling, C. Y. Lu, and J. W. Pan, On-Demand Single Photons with High Extraction Efficiency and Near-Unity Indistinguishability from a Resonantly Driven Quantum Dot in a Micropillar, *Phys. Rev. Lett.* **116**, 020401 (2016).
- [33] N. Tomm, A. Javadi, N. O. Antoniadis, D. Najer, M. C. Löbl, A. R. Korsch, R. Schott, S. R. Valentin, A. D. Wieck, A. Ludwig, and R. J. Warburton, A bright and fast source of coherent single photons, *Nat. Nanotechnol.* **16**, 399 (2021).
- [34] R. Uppu, F. T. Pedersen, Y. Wang, C. T. Olesen, C. Papon, X. Zhou, L. Midolo, S. Scholz, A. D. Wieck, A. Ludwig, and P. Lodahl, Scalable integrated single-photon source, *Sci. Adv.* **6**, eabc8268 (2020).
- [35] D. M. Jackson, D. A. Gangloff, J. H. Bodey, L. Zaporski, C. Bachorz, E. Clarke, M. Hugues, C. Le Gall, and M. Atatüre, Quantum sensing of a coherent single spin excitation in a nuclear ensemble, *Nat. Phys.* **17**, 585 (2021).
- [36] K. Sharman, F. K. Asadi, S. C. Wein, and C. Simon, Quantum repeaters based on individual electron spins and nuclear-spin-ensemble memories in quantum dots, *Quantum* **5**, 570, 2010.13863.
- [37] D. Buterakos, E. Barnes, and S. E. Economou, Deterministic generation of all-photonic quantum repeaters from solid-state emitters, *Phys. Rev. X* **7**, 041023 (2017).
- [38] A. Russo, E. Barnes, and S. E. Economou, Generation of arbitrary all-photonic graph states from quantum emitters, *New J. Phys.* **21**, 055002 (2019).
- [39] E. Hecht, *Optics*, 4th ed. (Addison Wesley, 2002).
- [40] C. Gerry and P. Knight, *Introductory Quantum Optics*, 1st ed. (Cambridge University Press, 2005).
- [41] B. Urbaszek, X. Marie, T. Amand, O. Krebs, P. Voisin, P. Maletinsky, A. Högele, and A. Imamoglu, Nuclear spin physics in quantum dots: An optical investigation, *Rev. Mod. Phys.* **85**, 79 (2013).
- [42] T. M. Godden, J. H. Quilter, A. J. Ramsay, Y. Wu, P. Brereton, S. J. Boyle, I. J. Luxmoore, J. Puebla-Nunez, A. M. Fox, and M. S. Skolnick, Coherent optical control of the spin of a single hole in an InAs/GaAs quantum dot, *Phys. Rev. Lett.* **108**, 017402 (2012).
- [43] A. Delteil, Z. Sun, W.-b. Gao, E. Togan, S. Faelt, and A. Imamoglu, Generation of heralded entanglement between distant hole spins, *Nature Physics* **12**, 218 (2016).
- [44] D. Ding, M. H. Appel, A. Javadi, X. Zhou, M. C. Löbl, I. Söllner, R. Schott, C. Papon, T. Pregolato, L. Midolo, A. D. Wieck, A. Ludwig, R. J. Warburton, T. Schröder, and P. Lodahl, Coherent optical control of a quantum-dot spin-qubit in a waveguide-based spin-photon interface, *Phys. Rev. Appl.* **11**, 031002 (2019).
- [45] C. K. Hong, Z. Y. Ou, and L. Mandel, Measurements of Subpicosecond Time Intervals between Two Photons by Interference, *Phys. Rev. Lett.* **59**, 2044 (1987).
- [46] P. Tighineanu, C. L. Dreeßen, C. Flindt, P. Lodahl, and A. S. Sørensen, Phonon Decoherence of Quantum Dots in Photonic Structures: Broadening of the Zero-Phonon Line and the Role of Dimensionality, *Phys. Rev. Lett.* **120**, 257401 (2018).
- [47] C. W. Chou, H. de Riedmatten, D. Felinto, S. V. Polyakov, S. J. van Enk, and H. J. Kimble, Measurement-induced entanglement for excitation stored in remote atomic ensembles, *Nature* **438**, 828 (2005), number: 7069 Publisher: Nature Publishing Group.
- [48] O. Gühne and G. Tóth, Entanglement detection, *Physics Reports* **474**, 1 (2009), publisher: Elsevier B.V.
- [49] M. H. Appel, *A Quantum Dot Source of Time-Bin Multi-Photon Entanglement*, *Phd thesis*, University of Copenhagen (2021).

- [50] A. V. Kuhlmann, J. Houel, A. Ludwig, L. Greuter, D. Reuter, A. D. Wieck, M. Poggio, and R. J. Warburton, Charge noise and spin noise in a semiconductor quantum device, *Nature Physics* **9**, 570 (2013), publisher: Nature Publishing Group.
- [51] L. Zhai, G. N. Nguyen, C. Spinnler, J. Ritzmann, M. C. Löbl, A. D. Wieck, A. Ludwig, A. Javadi, and R. J. Warburton, Quantum Interference of Identical Photons from Remote Quantum Dots, *arXiv:2106.03871* (2021).
- [52] <https://doi.org/10.17894/ucph.e0771d0b-b09a-45ae-a2a5-8e7a05fae115> .

Supplementary material for «Entangling a Hole Spin with a Time-Bin Photon: A Waveguide Approach for Quantum Dot Sources of Multi-Photon Entanglement»

Martin Hayhurst Appel¹, Alexey Tiranov¹, Simon Pabst¹, Ming Lai Chan¹, Christian Starup¹, Ying Wang¹, Leonardo Midolo¹, Konstantin Tiurev¹, Sven Scholz², Andreas D. Wieck², Arne Ludwig², Anders Søndberg Sørensen¹, and Peter Lodahl¹

¹Center for Hybrid Quantum Networks (Hy-Q), The Niels Bohr Institute, University of Copenhagen, DK-2100 Copenhagen Ø, Denmark

²Lehrstuhl für Angewandte Festkörperphysik, Ruhr-Universität Bochum, Universitätsstraße 150, 44801 Bochum, Germany

Contents

1	Sample	2
2	Experimental Setup	3
3	Time-Bin Interferometer	5
4	Optical Loss budget	8
5	Spin Dependent Optical Excitation	9
6	Spin Control	10
7	Hong-Ou-Mandel Visibility	12
8	Bell State Analysis	14
9	Monte Carlo Simulation	17
10	Three-Qubit GHZ Measurement	19
11	Effect of Spectral Diffusion and Blinking	21

1 Sample

Fig. S1 shows the quantum dot (QD) level diagram and an SEM picture of the measured waveguide device. The same QD was characterized in Ref. [1] where additional spectroscopic details are available. Details on sample growth and fabrication are presented in Ref. [2]. Key parameters of the positively charged QD are summarized in Table S1.

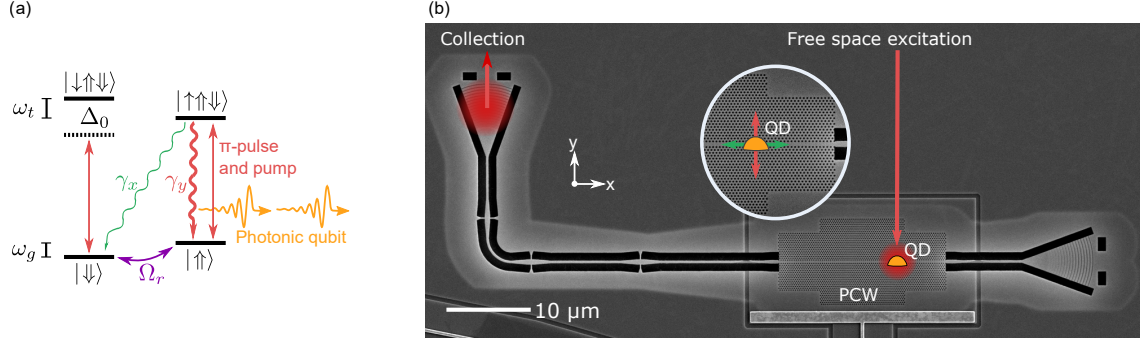


Figure S1: (a) Energy level diagram of a positively charged QD in a Voigt magnetic field. \downarrow, \uparrow denote hole spins and \uparrow, \downarrow denote electron spins. $\omega_{g(t)}$ is the ground(trion) Zeeman splitting and $\Delta_0 = \omega_g + \omega_t$. γ_x, γ_y are radiative decay rates and Ω_r is the effective spin Rabi frequency given by the Raman laser. (b) SEM image of the measured two-sided photonic crystal waveguide structure. The QD is addressed by lasers propagating from free space and the emitted photons are coupled into the waveguide mode, scattered out of the left grating coupler and coupled into a single-mode fiber.

Property	Value
Emission wavelength	945.0 nm
Trion decay rate $\gamma_0 = \gamma_x + \gamma_y$	$(2.48 \pm 0.02) \text{ ns}^{-1}$
Optical cyclicity $C = \gamma_y/\gamma_x$	14.7 ± 0.2
Transform-limited linewidth $\gamma/(2\pi)$	$(395 \pm 3) \text{ MHz}$
Measured linewidth	1050 MHz
Trion Zeeman splitting $\omega_t/(2\pi)$	9.6 GHz
Electron g-factor	0.34
Ground state Zeeman splitting $\omega_g/(2\pi)$	7.3 GHz
Hole g-factor	0.26
Spin dephasing time T_2^*	$(23.2 \pm 1.4) \text{ ns}$

Table S1: Key properties of the studied positively charged QD. All parameters are measured in a $B_y = 2 \text{ T}$ magnetic field.

2 Experimental Setup

An overview of the experimental setup is given in Fig. S2. Using a series of beamsplitters (BS), four lasers are combined and reflected into the cryostat. A polarizing beamsplitter (PBS) and a pair of half-waveplates (HWP) and quarter-waveplates (QWP) control the laser polarization in each path. Additionally, each laser path contains an acousto-optical modulator (AOM) to control the optical power. The four lasers comprise

1. Raman laser used for spin rotations. The CW laser is amplitude modulated by a fiber-coupled electro-optical modulator (EOM) to add sidebands matching the hole spin Zeeman splitting [3]. By combining a microwave source, a variable phase shifter and a microwave of/off-switch, we create microwave pulses that drive the EOM. Additionally, an AOM is used to stabilize the optical power.
2. Pumping laser used for spin initialization and readout. The CW laser is modulated by an AOM to create pulses (8 ns rise time).
3. 830 nm laser used to initialize the hole charge state. The CW laser is modulated by an AOM to create pulses (30 ns rise time). A 100 ns pulse is placed at the end of the entanglement pulse sequence to initialize a hole spin for the next round of the experiment.
4. Pulsed laser used for optical π -pulses. A mode-locked Ti-Sapphire laser creates 5 ps pulses at a 72 MHz repetition rate. The pulses are stretched in time to $T_{opt} = 35$ ps using a volume Bragg grating (VBG) and an AOM is used to pick out a single pulse. This pulse is doubled using the excitation-pass of the TBI (detailed in section 3) before being combined with the other lasers.

As the pulsed laser has a fixed repetition rate it constitutes the experimental clock to which all other devices are phase-locked. This is achieved with a custom FPGA solution. A photodiode detects the 72 MHz pulse train and drives a phase-locked loop (PLL) in the FPGA. The PLL drives a series of pulse generators within the FPGA which deliver TTL pulses to the modulators and the time tagger (see Fig. S2).

Photon detection is achieved with a pair of superconducting nanowire single-photon detectors (SNSPDs) with 70-90% quantum efficiency, and a Swabian Ultra time tagger is used to record the photon detection times and the FPGA synchronization pulses. Detector dark counts ~ 1 Hz are completely negligible. Detector time jitter (~ 100 ps RMS) is irrelevant as the time-bin protocol only requires the photonic detection windows (2 ns duration) to be resolved.

The sample itself is held at 4.2 K inside a closed-cycle cryostat. A superconducting vector magnet provides the 2 T in-plane magnetic field. The sample is imaged with a 0.81 NA objective and 3 piezo positioners are used to translate the sample and bring it into focus of the objective. Additionally, a DC voltage source provides a bias voltage V_{bias} to the sample. This in conjunction with the 830 nm laser facilitates positive charging of the QD [1].

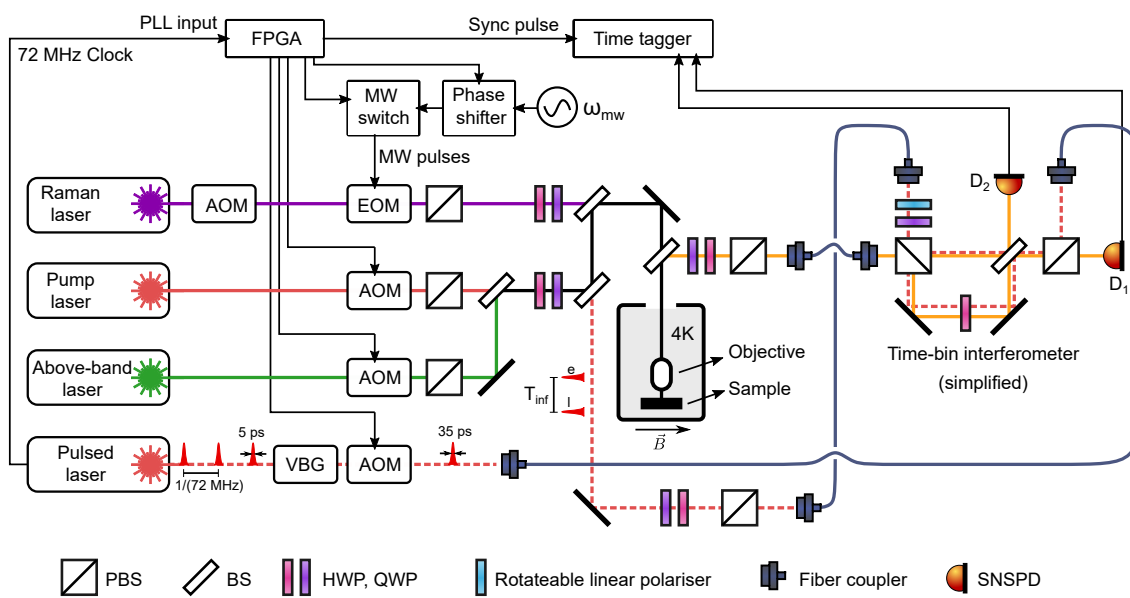


Figure S2: Experimental setup.

3 Time-Bin Interferometer

The full layout of the time-bin interferometer (TBI) is shown in Fig. S3. It contains a detection-pass for measuring the time-bin photon and an excitation-pass for generating the early and late excitation pulses. The long arm of the interferometer comprises a 3.54 m free space delay resulting in a $T_{inf} = 11.8$ ns delay.

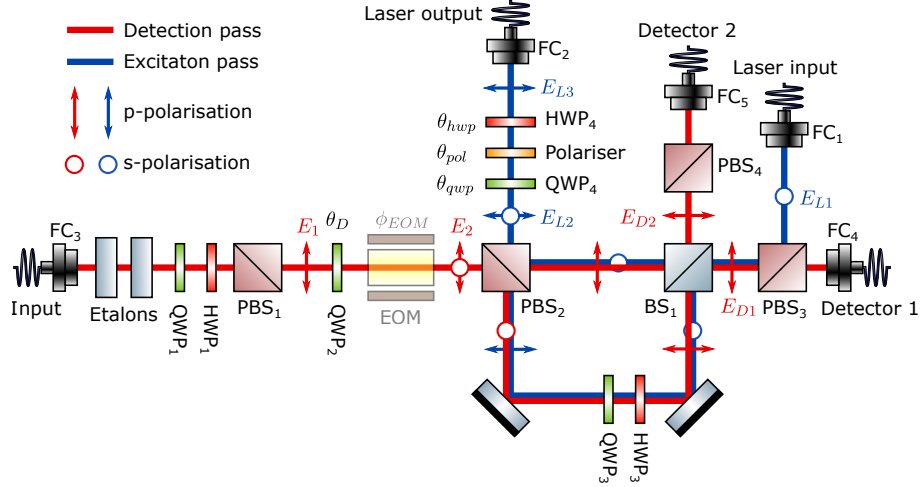


Figure S3: Double pass time-bin interferometer. The excitation-pass (blue) doubles the laser pulse inserted in FC₁. The detection-pass (red) applies frequency filtering and interferes early and late pulses leading to detection in FC₄ or FC₅. QWP₂ and a free space EOM set the splitting ratio of PBS₂ and may be used for active photon routing. Lenses and additional mirrors are excluded for clarity.

3.1 Working Principle

The detection-pass begins with two identical etalons with 3 GHz linewidth and 100 GHz free spectral range. The etalons are resonant with the $|\uparrow\rangle \leftrightarrow |\uparrow\downarrow\rangle$ transition and transmit the time-bin photon but provide rejection of the Raman laser (spectrally located between two longitudinal etalon modes), phonon sideband, and emission from the other three optical transitions of the QD. After the etalons, a pair of waveplates and PBS₁ fix the photon polarization. Next, a free-space EOM and QWP₂ set the splitting ratio of PBS₂. The EOM can be used to enable active switching but was not driven in the reported measurement. Instead, the EOM provided a constant birefringence and QWP₂ was rotated to achieve a 50/50 splitting ratio of PBS₂. After PBS₂ the time-bin photon interferes with itself on BS₁. Waveplates in the long arm ensure identical polarization of the beams impeding on BS₁. Finally, the time-bin photon is coupled into fiber couplers FC₄ and FC₅ which lead to two SNSPD detectors.

In the excitation-pass a single laser pulse is emitted from FC₁ and injected into the TBI via PBS₃. On encountering BS₁ the pulse is divided. The long interferometer arm creates the late pulse which becomes p-polarized thanks to HWP₃ and QWP₃. After being recombined by PBS₂, the early and late pulses have electric field amplitudes proportional to

$$\mathbf{E}_{L2}^e = \sqrt{T_{\text{short}}} \begin{pmatrix} 0 \\ 1 \end{pmatrix}, \quad (1)$$

$$\mathbf{E}_{L2}^l = \sqrt{T_{\text{long}}} e^{i\phi'} \begin{pmatrix} 1 \\ 0 \end{pmatrix}, \quad (2)$$

where the $e(l)$ superscripts denote early(late), and $T_{\text{short(long)}}$ is the intensity transmission coefficients of the short(long) arm including the BS₁ splitting ratio and other losses. ϕ' is the relative phase accumulated in the long arm and $\begin{pmatrix} 1 \\ 0 \end{pmatrix}$ and $\begin{pmatrix} 0 \\ 1 \end{pmatrix}$ denotes p- and s-polarization, respectively. The orthogonal polarizations enable us to set a programmable phase shift using QWP₄, a linear polarizer and HWP₄. These three elements are described by the total Jones matrix [4]

$$M_{\text{tot}} = M_{\text{hwp}}(\theta_{\text{pol}}/2)M_{\text{pol}}(\theta_{\text{pol}})M_{\text{qwp}}(\theta_{\text{qwp}}) \quad (3)$$

$$= \left(\frac{1+i}{2} \right) \begin{bmatrix} \cos(\theta_{\text{pol}}) - i \cos(\theta_{\text{pol}} - 2\theta_{\text{qwp}}) & \sin(\theta_{\text{pol}}) + i \sin(\theta_{\text{pol}} - 2\theta_{\text{qwp}}) \\ 0 & 0 \end{bmatrix}, \quad (4)$$

where θ_{pol} and θ_{qwp} denote the polarizer transmission axis and QWP fast axis with respect to horizontal, respectively. The HWP angle is set to always ensure a p-polarized output. Multiplying Eq. (4) onto Eq. (1) and Eq. (2) gives the electric fields at FC₂

$$E_{L3}^e = \left(\frac{1+i}{2} \right) \sqrt{T_{\text{short}}} (\sin(\theta_{\text{pol}}) + i \sin(\theta_{\text{pol}} - 2\theta_{\text{qwp}})), \quad (5)$$

$$E_{L3}^l = \left(\frac{1+i}{2} \right) e^{i\phi'} \sqrt{T_{\text{long}}} (\cos(\theta_{\text{pol}}) - i \cos(\theta_{\text{pol}} - 2\theta_{\text{qwp}})). \quad (6)$$

By choosing $\theta_{\text{qwp}} = \pi/4$ and $T_{\text{short}} = T_{\text{long}}$, the two pulses achieve equal intensity and a phase difference of

$$\phi_e = \arg(E_{L3}^e) - \arg(E_{L3}^l) = \phi' + 2\theta_{\text{pol}} - \pi/2. \quad (7)$$

In essence, the detection pattern depends on the phase of the detection interferometer ϕ_d and the phase of the excitation interferometer ϕ_e . They are mutually phase-stable, as the two passes encounter the same optics. However, by scanning θ_{pol} an additional controllable phase can be added, which is enough to effectively scan the interferometer.

In practice, we achieve $T_{\text{short}} = T_{\text{long}}$ by manipulating the optical coupling into FC₂ and exploiting that the short and long paths do not have perfect spatial overlap at FC₂.

The excitation and detection-passes are in general orthogonally polarized and displaced 3 mm vertically resulting in low levels of cross-talk. We estimate that only one in $\approx 2 \cdot 10^{11}$ excitation photons are reflected into a detector. This is sufficient, although some reflections are visible in the entanglement data (main text Fig. 1e).

3.2 Interferometer Characterization

We now verify the stability and visibility of the TBI. To do so, a pair of early/late excitation pulses is generated by the TBI, reflected of the sample surface and coupled into the TBI detection-pass. This procedure is equivalent to connecting fiber couplers FC₂ and FC₃ in Fig. S3. We define the detector contrast $C = (I_1^m - I_2^m)/(I_1^m + I_2^m)$ where I_i^m is the intensity of detector i within the middle detection window. Fig. S4 shows how the intensities are extracted from a histogram and Fig. S5 shows $C(\theta_{\text{pol}})$ for two separate measurements taken 142 hours apart without intermediate alignment. The detector contrast is fit with the model

$$C(\theta_{\text{pol}}) = \nu_{\text{TBI}} \sin(2(\theta_{\text{pol}} - \theta_0)) \quad (8)$$

and estimates near-perfect visibilities of $\nu_{\text{TBI}} = 99.7\%$ and $\nu_{\text{TBI}} = 99.9\%$ for series 1 and series 2, respectively. Furthermore, the fringe phase θ_0 only shifts by $(4.1 \pm 0.2)^\circ$ between the two measurements. The 5 minutes required to calibrate θ_0 are negligible compared to the duration of stability, and the TBI is thus self-stabilizing for our purposes. Slight systematic deviations from the fit are visible in Fig. S5 owing to a $\sim 5\%$ variation in the relative intensity of the early and late pulses as a function of θ_{pol} .

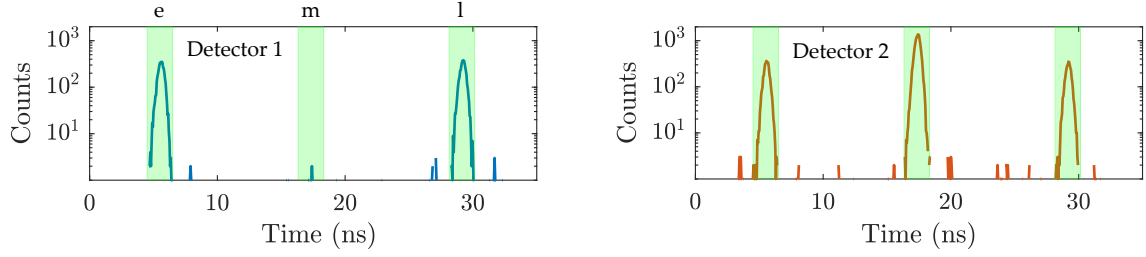


Figure S4: Histograms recorded from both TBI detectors showing excitation pulses reflected of the sample. The early(e), middle(m) and late(l) detection windows are 2 ns long and marked in green. The applied θ_{pol} setting corresponds to series 1 minimum in Fig. S5 and yields a near-zero intensity in the middle window of detector 1.

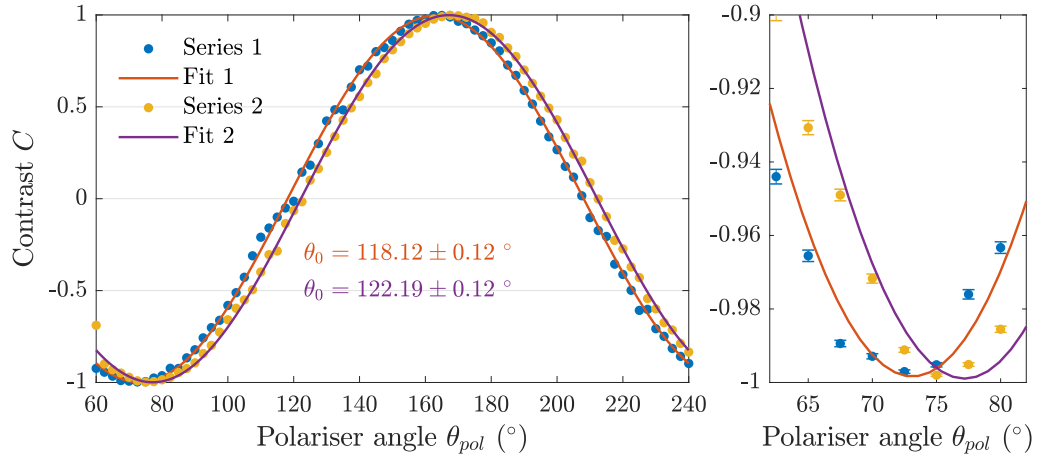


Figure S5: Detector contrast for different values of θ_{pol} . The right subplot shows a data zoom in. Errorbars are derived from shot noise. Fits following Eq. (8) are used to estimate the fringe phase and the TBI visibility.

4 Optical Loss budget

Table S2 gives an estimated loss budget for the entanglement experiment and predicts a total loss of 20.2 dB. In comparison, the $g^{(2)}$ experiment (main text) yields a 0.282% (25.5 dB loss) single-photon detection efficiency, and we thus have 5 dB of unaccounted loss. These losses may be due to device fabrication imperfections such as over-etched grating couplers [5]. The two-sided nature of the PCW and the 50/50 BS in the collection path (Fig. S2) constitute the main losses. Additional improvements may be gained by adding distributed Bragg reflectors to the gratings as discussed in Ref. [2].

Loss source	Efficiency (%)	Loss (dB)	Source/assumptions
Sample			
Hole spin initialization	75	1.25	Blinking measurements
Zero-phonon line emission	90	0.46	[6]
Branching efficiency ¹	88	0.56	[1]
Two-sided PCW	50	3.01	Equal left/right coupling
Nanobeam interfaces	96	0.18	[2]
Grating coupler diffraction efficiency ²	60	2.22	[2]
Sum		7.68	
Cryostat optics			
Optical inset ³	75	1.25	Measured
50/50 BS	49	3.10	Measured
Polarization optics	85	0.71	Measured
Collection fiber coupling	60	2.22	Measured
Sum		7.27	
Interferometer			
Two fiber matings	76	1.19	Measured
Etalon filtering ⁴	73	1.37	Measured
Interferometer optics	80	0.97	Measured
Interferometer fiber coupling	84	0.76	Measured
SNSPD detectors	80	0.97	Manufacturer specifications
Sum		5.25	
Total loss		20.2	

Table S2: Estimated experimental loss budget. ¹ The probability of the photon being emitted via the cycling transition and being emitted into the waveguide mode. ² The probability of the photon being scattered into the microscope objective. This does not include the mode overlap with the collection fiber. ³ Microscope objective and lenses in 4F-system. ⁴ Includes scattering losses and spectral overlap between a zero-phonon line photon and the etalon system. Phonon sideband losses are noted separately.

5 Spin Dependent Optical Excitation

We now explicitly demonstrate that the detection of a photon is strongly conditioned on the QD spin state. The same magnetic field $B_y = 2$ T is applied as in the main experiment and the spin is prepared in $|\downarrow\rangle$ ($|\uparrow\rangle$) by optically pumping into $|\downarrow\rangle$ and applying a $0(1\pi)$ spin rotation. The QD is then excited by a single 35 ps excitation pulse resonant with $|\uparrow\rangle \leftrightarrow |\uparrow\downarrow\uparrow\rangle$ and the QD emission intensity is measured using the short arm of the TBI.

Fig. S6a shows the emission intensity as a function of spin state and excitation power P . Given initialization in $|\uparrow\rangle$, the measured intensity I_{\uparrow} is well fit by two-level Rabi-flopping [7]

$$I_{\uparrow}(P) = I_{max} \times \sin\left(\frac{\pi}{2}\sqrt{\frac{P}{P_{\pi}}}\right)^2, \quad (9)$$

where I_{max} is the maximum intensity and P_{π} is the π -pulse power. The fit in Fig. S6a provides an estimate of P_{π} which is used for the remaining experiments

Preparing $|\downarrow\rangle$ results in the intensity $I_{\downarrow} \ll I_{\uparrow}$. For the five lowest powers, the ratio of intensities has an average value $\langle I_{\uparrow}/I_{\downarrow} \rangle \approx 45$ which is consistent with the limit set by the spin initialization fidelity.

Additionally, the laser background I_{bg} can be estimated by applying a non-resonant V_{bias} which renders the QD optically inactive. The laser extinction ratio I_{\uparrow}/I_{bg} is given in Fig. S6b and reaches a value of ≈ 240 at $P = P_{\pi}$. The extinction is sensitive to the exact optical alignment and varies slightly between data sets.

In summary, the QD emission under pulsed excitation is seen to be highly spin-dependent, has the dynamics of a single two-level system, and exhibits low levels of laser background.

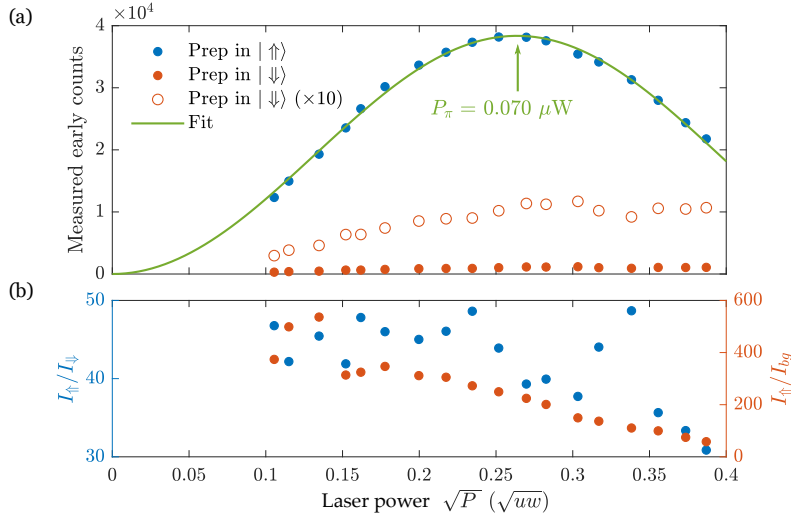


Figure S6: QD fluorescence under pulsed excitation as a function of laser pulse power P and QD spin state using a $B_y = 2$ T magnetic field. **(a)** Spin state dependent fluorescence. The fit follows Eq. (9). **(b)** Left y-axis: Ratio between fluorescence intensities conditioned on spin state. Right y-axis: Fluorescence given $|\uparrow\rangle$ divided by laser background.

6 Spin Control

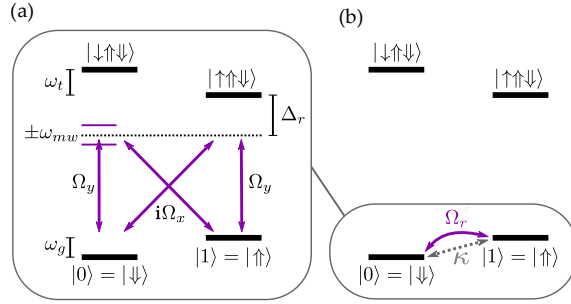


Figure S7: Raman level scheme. **(a)** A detuned, circularly polarized laser drives a two-photon Raman transition between the heavy-hole ground states of a positively charged QD. Δ_r is the optical detuning, $\omega_g(\omega_t)$ is the ground state(trion) Zeeman splitting and Ω_x, Ω_y are the optical Rabi frequencies of the x and y -dipoles. **(b)** Effective spin dynamics with spin Rabi frequency Ω_r and spin-flip rate κ .

Spin control follows the level scheme in Fig. S7. A circularly polarized Raman laser drives all four linear optical dipoles and is detuned by $\Delta_r = 2\pi \times 350$ GHz from $|\uparrow\uparrow\downarrow\rangle$. An amplitude modulating EOM (Fig. S2) driven at frequency ω_{mw} creates two sidebands detuned $\pm\omega_{mw}$ from the fully suppressed carrier. The coherent evolution of the ground states is given by [3]

$$\hat{H}_{rot} = \begin{bmatrix} -\delta/2 & \frac{\Omega_r}{2} e^{-2i\phi_{mw}} \\ \frac{\Omega_r}{2} e^{2i\phi_{mw}} & \delta/2 \end{bmatrix}, \quad (10)$$

where $\Omega_r = \Omega_x \Omega_y^* / \Delta_r$ is the real, effective spin Rabi frequency, $\delta = \omega_g - 2\omega_{mw}$ is the two-photon detuning and ϕ_{mw} is the modulation phase. By toggling a phase switch with the FPGA (Fig. S2), ϕ_{mw} can be switched between two arbitrary values on a ns-timescale. This provides control over the rotation axis of the final \hat{R}_i rotation pulse.

6.1 Quality of Rotation Pulses

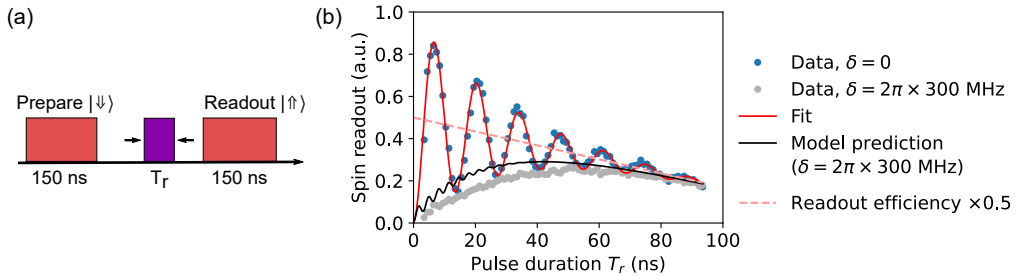


Figure S8: Spin Rabi oscillations. **(a)** Experimental pulse sequence. **(b)** Intensity of spin readout proportional to the population of $|\uparrow\uparrow\rangle$. The pulse duration is varied for two values of δ . The damped oscillations are fitted (red line) with Eq. (14). The dashed line indicates the modelled readout efficiency.

To estimate the rotation pulse fidelity we employ the prepare-rotate-readout sequence of Fig. S8a to observe the spin Rabi oscillations in Fig. S8b. We employ the same optical power and Δ_r as in the entanglement experiment. The measurement series with $\delta = 0$ exhibits clear

dampened Rabi oscillations which we fit with a master equation including effects from both inhomogeneous broadening and spin-flips. We represent the heavy-hole spin states $\{|\downarrow\rangle, |\uparrow\rangle\}$ as $\{|0\rangle, |1\rangle\}$ and take the evolution of the density matrix $\hat{\rho}$ to follow the Lindblad master equation

$$\frac{d}{dt}\hat{\rho} = -i[\hat{H}_{rot}, \hat{\rho}] + \sum_{j=1}^2 \left[\hat{C}_j \hat{\rho} \hat{C}_j^\dagger - \frac{1}{2}(\hat{C}_j^\dagger \hat{C}_j \hat{\rho} + \hat{\rho} \hat{C}_j^\dagger \hat{C}_j) \right], \quad (11)$$

where \hat{H}_{rot} is given by Eq. (10). Spin-flips are incorporated via the collapse operators $\hat{C}_1 = \sqrt{\kappa}|0\rangle\langle 1|$ and $\hat{C}_2 = \sqrt{\kappa}|1\rangle\langle 0|$ where κ is the spin-flip rate. κ is assumed equal for both operators as the Zeeman energy $\hbar\omega_g = h \times 7.3$ GHz is small compared to the thermal energy $k_B T \approx h \times 80$ GHz. Eq. (11) gives rise to the equations of motion

$$\frac{d}{dt} \begin{pmatrix} \rho_{00} \\ \rho_{01} \\ \rho_{10} \\ \rho_{11} \end{pmatrix} = \begin{pmatrix} -\kappa & \frac{i\Omega_r}{2} & -\frac{i\Omega_r}{2} & \kappa \\ \frac{i\Omega_r}{2} & -\kappa + i\delta & 0 & -\frac{i\Omega_r}{2} \\ -\frac{i\Omega_r}{2} & 0 & -\kappa - i\delta & \frac{i\Omega_r}{2} \\ \kappa & -\frac{i\Omega_r}{2} & \frac{i\Omega_r}{2} & -\kappa \end{pmatrix} \begin{pmatrix} \rho_{00} \\ \rho_{01} \\ \rho_{10} \\ \rho_{11} \end{pmatrix}, \quad (12)$$

for $\phi_{mw} = 0$. Using the initial state $\hat{\rho} = |0\rangle\langle 0|$, Eq. (12) is integrated over the pulse duration T_r to yield the $\rho_{11}(T_r)$ population. We assume the sidebands to be on resonance such that $\delta \rightarrow \delta_{OH}$ where δ_{OH} is the two-photon detuning caused by the quasi-static [8] nuclear Overhauser field¹. This broadening is incorporated by performing the integral

$$\langle \rho_{11}(T_r; \Omega_r, \kappa) \rangle_{inhom} = \int_{-\infty}^{\infty} d\delta_{OH} \rho_{11}(T_r; \Omega_r, \kappa, \delta_{OH}) \frac{e^{-\delta_{OH}^2/(2\sigma^2)}}{\sigma\sqrt{2\pi}}, \quad (13)$$

where $\sigma = \sqrt{2}/T_2^*$ is the RMS fluctuation of δ_{OH} and is fixed according to the independently measured $T_2^* = (23.2 \pm 1.3)$ ns which is largely comparable with hole spins in bulk QDs [9, 11, 12]. Finally, the master equation is related to the measured intensity via

$$I(T_r) = I_0(1 - \alpha T_r) \langle \rho_{11}(T_r; \Omega_r, \kappa) \rangle_{inhom}, \quad (14)$$

where α is an empirical parameter associated with a T_r -dependent reduction in readout efficiency. The model provides an excellent fit of the data (red line in Fig. S8b) and estimates $\Omega_r = 2\pi \times 72$ MHz and $\kappa = 0.018$ ns⁻¹. Evaluating ρ_{11} after a 1π -oscillation estimates a π -pulse fidelity of $F_\pi = 88.5\%$. The infidelity owing to inhomogeneous broadening can be quantified according to $1 - F_\pi^{deph} \approx 1/(\Omega_r T_2^*)^2 = 1.8\%$. Hence, we attribute the remaining $\approx 10\%$ infidelity to κ , which is by far the main cause of dampening. In summary, we distinguish between κ and δ_{OH} induced dampening by applying a master equation approach, fixing T_2^* based on independent measurements and keeping κ as a free fitting parameter.

We justify the inclusion of α by noting that spin readout for $\delta = 2\pi \times 300$ MHz (Fig. S8b) starts to decrease for long T_r . For $\delta \gg \Omega_r$, the dynamics are dominated by spin-flips and populations evolve monotonously according to Eq. (12). Thus, the observed decrease in $I(T_r)$ cannot be attributed to spin-flips and is thus an indication of a modulated readout efficiency. This is compatible with the "power tuning" observed in all our devices [13] where an increase in optical power shifts the optical resonances, possibly due to optically generated charge carriers. The choice of a linearly decreasing readout efficiency is somewhat ad-hoc and leads to negative efficiencies for long T_r but has the benefit of only adding one additional fitting parameter. Using

¹In addition to nuclear noise, charge noise also gives a slow inhomogeneous broadening of hole spins [9, 10]. However, the measurement performed here can not distinguish between the two.

the fitted values of Ω_r, κ, α and setting $\delta = 2\pi \times 300$ MHz produces the black curve in Fig. S8b, which shows limited agreement with data for short T_r . This motivates further measurements of κ but does not alter the conclusion, namely that T_2^* alone cannot explain the poor π -pulse fidelity which considerably impacts the entanglement experiment (see section 9).

7 Hong-Ou-Mandel Visibility

We now elaborate on the estimation of the Hong-Ou-Mandel (HOM) visibility. Here, the spin is prepared in $|\uparrow\rangle$ and the QD is excited twice resulting in two separable photons (early and late) within the 606 ns repetition time. $g^{(2)}$ and HOM are estimated from the same 20-minute acquisition.

Most HOM estimates rely on varying the degree of two-photon interference, either by varying the temporal overlap [14] or by varying the photon polarization [2]. Since the TBI does not give access to these degrees of freedom, we instead follow the method of Ref. [15] in which two photons are injected into an unbalanced Michelson interferometer that closely resembles the TBI. The raw HOM visibility is calculated from

$$\mathcal{V}_{hom}^{raw} = 1 - \frac{N_{m1,m2}}{(N_{m1,e2} + N_{m2,e1} + N_{m1,l2} + N_{m2,l1})/2}, \quad (15)$$

where $N_{ij,kl}$ is the number of coincidences between a photon in detection window i and detector j and a second photon in detection window k and detector l , with both photons being detected within the same experimental repetition. In other words: Coincidences between both detectors at the middle bin are normalized to the coincidences between a middle and non-middle detection.

Following Ref. [15], we consider two mechanism which may reduce the HOM visibility of a perfect source of indistinguishable photons. Firstly, the signal photons may be mixed with noise photons which are fully distinguishable from the signal photons. Secondly, the detection interferometer may be imperfect. In the presence of these errors an ideal source will result in the measured visibility

$$\mathcal{V}_{hom}^{ideal} = 1 - \frac{R_P T_P [(g^{(2)} + 1)(R^2 + T^2) - 2RT\mathcal{V}_{TBI}^2]}{RT(R_P^2 + T_P^2)(g^{(2)} + 1)}, \quad (16)$$

where we use the shorthand notation $g^{(2)} = g^{(2)}(0)$, \mathcal{V}_{TBI} is the classical visibility of the TBI, $R(T)$ is the reflection(transmission) of BS_1 (Fig. S3) and $R_P(T_P)$ is the reflection(transmission) of the input photons incident on PBS_1 (Fig. S3). Reflection and transmission coefficients are with respect to power and are measured with a power meter. Eq. (16) differs slightly from Ref. [15] as our interferometer utilizes two beamsplitters with independent splitting ratios. We also emphasize that Eq. (16) assumes $g^{(2)} > 0$ to result from noise photons which are distinguishable from the ideal single photons. This assumption has been experimentally justified in some cases [16] but we do not investigation the assumption here.

The corrected visibility is then given by

$$\mathcal{V}_{hom}^{corr} = \frac{\mathcal{V}_{hom}^{raw}}{\mathcal{V}_{hom}^{ideal}}. \quad (17)$$

and represents the HOM visibility in the limit of a perfect interferometer and $g^{(2)} = 0$.

The data yield a raw visibility of $\mathcal{V}_{hom}^{raw} = 86.5 \pm 0.7\%$. Applying Eq. (17) and the $\mathcal{V}_{hom}^{ideal}$ estimated in Table S3 yields the corrected value $\mathcal{V}_{hom}^{corr} = 95.7 \pm 0.8$. The residual distinguishability can be attributed to elastic phonon scattering [17].

Correction	Experimental values	Visibility reduction $1 - \mathcal{V}_{hom}^{ideal}$
Splitting ratio	$R_P = 0.485$, $T_P = 0.515$, $R = 0.513$, $T = 0.487$	0.14%
Classical TBI visibility	$\mathcal{V}_{TBI} = 0.997$	0.60%
Intensity autocorrelation	$g^{(2)} = 0.047$	9.0%
Total reduction		9.7%

Table S3: Correction factors used to calculate $\mathcal{V}_{hom}^{ideal}$.

Finally, we elucidate a small detail in the $g^{(2)}$ measurement in Fig. 3b of the main text. At long delays the rate of late photon coincidences amounts to 88.4% of the rate of early photon coincidences. This difference can be attributed to the fact that a late photon is conditioned on the early emission occurring via the cycling transition with probability $C/(C + 1)$. The coincidence probability for two late photons is thus scaled by $(C/(C + 1))^2 = (87.7 \pm 0.2)\%$ relative to the early case in close agreement with the experiment.

8 Bell State Analysis

Here we explicitly describe the procedure used to estimate the Bell state fidelity with and without background correction. When analyzing the acquired photon time-tags, we post-select on observing at least one click in the photonic detection windows and at least one click in the spin readout window. Due to the low detection efficiency, the probability of observing multiple photons in the photonic windows is negligible.

8.1 Background Correction

To estimate a background-free detection pattern, we consider the observed photons to be either signal photons originating from the QD or uncorrelated background photons. We then assume the number of observed coincidences to follow

$$N_{\text{observed}} = N_{\text{true}} + M_{\text{rep}} [P(b_p)P(b_r) + P(b_p)P(s_r) + P(s_p)P(b_r)], \quad (18)$$

where N_{true} is the number of coincidences owing to two signal photons, M_{rep} is the number of experimental repetitions and the $P()$ terms represent the probability of observing a signal(s) or a background(b) photon occurring in a photonic detection window (p-subscript) or the spin readout window (r-subscript). Thus, the last three terms in Eq. (18) represent combinations of signal and background resulting in false coincidences. We estimate these terms as $P(a) = N_a/M_{\text{rep}}$ where N_a is the number of detections of type a . Inserting in Eq. (18) and rearranging the terms gives an estimate of the true number of coincidences

$$\langle N_{\text{true}} \rangle = N_{\text{observed}} - \frac{1}{M_{\text{rep}}} (N(b_p)N(b_r) + N(b_p)N(s_r) + N(s_p)N(b_r)). \quad (19)$$

We consider three different sources of background photons:

1. Laser scatter from the excitation laser (already discussed in section 5).
2. Raman pulses. The Raman laser is spectrally located at the transmission minimum of the etalons and scatter from this laser is effectively rejected. However, the QD may emit fluorescence during the Raman pulses owing to a finite trion population. This is evident from Fig. S9 where the Raman pulses are only evident at a resonant V_{bias} . The Raman pulses do not themselves overlap with the photon emission in time. However, when measured through the TBI, the pulses are doubled in time and some overlap occurs. This overlap is most pronounced when projecting the spin onto $|\downarrow\rangle$ for which a $\hat{R}_i = \hat{R}_y(\pi)$ rotation is applied after the late excitation (see Fig. S9).
3. The pumping laser produces a small amount of laser scatter in the spin readout.

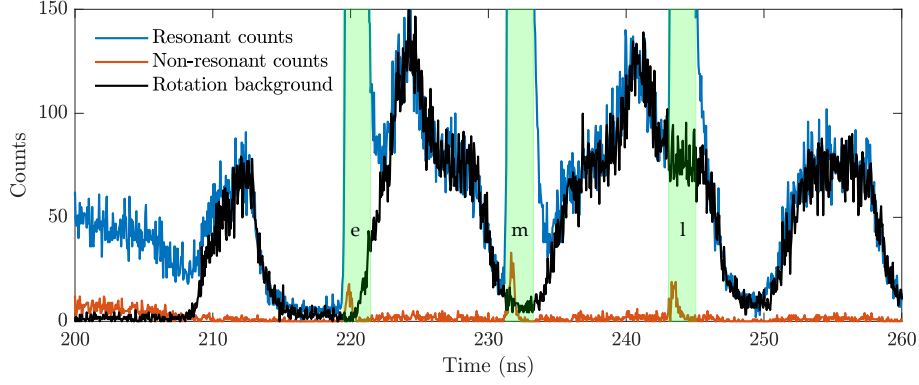


Figure S9: Sources of background during the photonic detection windows. Blue (red) curves show fluorescence histograms from the full entanglement experiment using a $\hat{R}_i = \hat{R}_y(\pi)$ spin rotation and a resonant (non-resonant) V_{bias} . The blue curve extends up to 2000(4000) counts during the $e(m)$ window. The black curve shows fluorescence generated by the rotation laser at resonant V_{bias} . All histograms were acquired over 30 s. Green windows represent the e, m, l detection windows. Especially the l window is contaminated by rotation background.

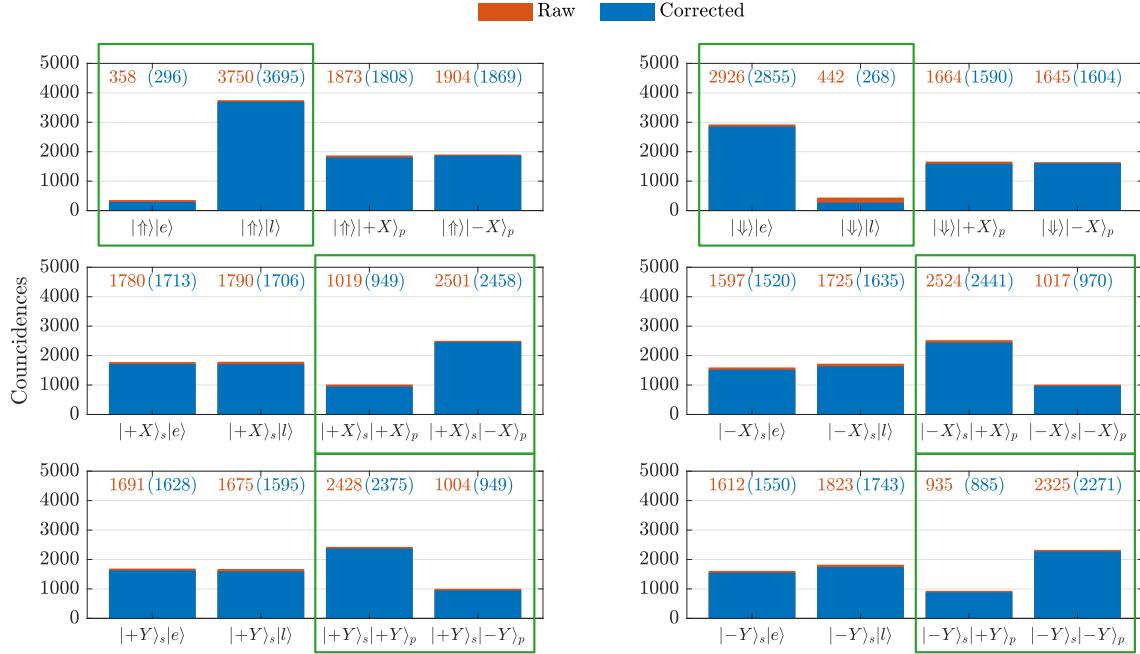


Figure S10: Coincidence counts from the six measurement settings used to characterize the Bell state. The x-labels denote the measured spin and photon projectors. A 60 s integration time was applied for each of the six measurement setting.

8.2 Fidelity Estimation

Fig. S10 shows the number of spin-photon coincidences with and without background correction. Measuring the \hat{P}_z , \hat{M}_x and \hat{M}_y operators requires six measurement settings as only one spin-projector can be measured at a time. As the photonic basis is selected randomly, only half of the outcomes (green boxes in Fig. S10) are used to construct Fig. 2a,c in the main text. The operators of interest and the Bell state fidelity [18] are calculated according to

$$\langle \hat{P}_z \rangle = \frac{N_{\downarrow,e} + N_{\uparrow,l}}{N_{\downarrow,e} + N_{\uparrow,l} + N_{\uparrow,e} + N_{\downarrow,l}}, \quad (20)$$

$$\langle \hat{M}_x \rangle = \frac{N_{+X,+X} + N_{-X,-X} - N_{+X,-X} - N_{-X,+X}}{N_{+X,+X} + N_{-X,-X} + N_{+X,-X} + N_{-X,+X}}, \quad (21)$$

$$\langle \hat{M}_y \rangle = \frac{N_{+Y,+Y} + N_{-Y,-Y} - N_{+Y,-Y} - N_{-Y,+Y}}{N_{+Y,+Y} + N_{-Y,-Y} + N_{+Y,-Y} + N_{-Y,+Y}}, \quad (22)$$

$$\langle \hat{\chi} \rangle = \frac{\langle \hat{M}_y \rangle - \langle \hat{M}_x \rangle}{2}, \quad (23)$$

$$\mathcal{F}_{Bell} = \frac{\langle \hat{P}_z \rangle + \langle \hat{\chi} \rangle}{2}, \quad (24)$$

where the N refers to the number of observations in Fig. S10. The "+" and "-" photon states correspond to measuring the photon on detector 1 and 2 in the middle detection window, respectively. The photon measurement basis is switched between X and Y by increasing θ_{pol} by $\pi/4$ corresponding to a $\pi/2$ change of the interferometer phase. The operator estimates and \mathcal{F}_{Bell} are given in Table S4 with and without background subtraction.

	Ideal value	Raw value	Corrected value
$\langle \hat{P}_z \rangle$	1	0.893 ± 0.004	0.921 ± 0.004
$\langle \hat{M}_x \rangle$	1	0.423 ± 0.011	0.437 ± 0.011
$\langle \hat{M}_y \rangle$	-1	-0.421 ± 0.011	-0.434 ± 0.011
$\langle \hat{\chi} \rangle$	1	0.422 ± 0.008	0.436 ± 0.008
\mathcal{F}_{Bell}	100%	$(65.7 \pm 0.4)\%$	$(67.8 \pm 0.4)\%$

Table S4: Fidelity estimates with and without background correction. Uncertainties denote 1σ errors derived from Poissonian statistics.

8.3 Alternative estimates

We have thus far proven spin-photon entanglement by estimating the fidelity to a Bell state using a limited set of measurements. This method is motivated by the fact that it will allow efficient fidelity estimates of N -qubit GHZ states using only $N + 1$ measurement settings (provided both spin-projections can be detected from one setting). However, to facilitate comparison with the existing literature, we also estimate the negativity and concurrence of the measured Bell state. Since the performed measurements do not constitute a full tomography we follow Ref. [19] and assume the spin-photon density matrix to take the form

$$\hat{\rho} = \begin{pmatrix} \rho_{00,00} & 0 & 0 & \rho_{00,11}e^{i\phi} \\ 0 & \rho_{01,01} & 0 & 0 \\ 0 & 0 & \rho_{10,10} & 0 \\ \rho_{00,11}e^{-i\phi} & 0 & 0 & \rho_{11,11} \end{pmatrix}, \quad (25)$$

where all ρ are real. The diagonal elements are extracted from the top row of Fig. S10. For the off-diagonal elements in Eq. (25), we use the relation [18]

$$\langle \hat{\chi} \rangle = Tr\{\hat{\rho}(|00\rangle\langle 11| + |11\rangle\langle 00|)\} = 2 \cos(\phi)\rho_{00,11}, \quad (26)$$

where $\langle \hat{\chi} \rangle$ is the experimentally measured visibility. Thus, Eq. (26) provides a lower bound estimate of $\rho_{00,11} \geq \langle \hat{\chi} \rangle / 2$.

Using the raw, uncorrected measurements we estimate the entanglement concurrence \mathcal{C} and negativity \mathcal{N} according to their standard definitions [20] and find

$$\mathcal{C} \geq 0.316 \pm 0.008, \quad (27)$$

$$\mathcal{N} \geq 0.158 \pm 0.004, \quad (28)$$

with uncertainties calculated from resampling the measurement outcomes. We note that the estimated quantities represent lower bounds, partly due to the lower bound of $\rho_{00,11}$, and partly due to the fact, that additional non-zero off-diagonal elements in Eq. (25) will increase \mathcal{C} and \mathcal{N} without affecting the performed measurements.

9 Monte Carlo Simulation

In this section, we briefly describe the infidelity mechanisms considered in our Monte Carlo (MC) simulation of the Bell state generation. We consider eight errors of which three relate to the intrinsic level structure of the QD. These errors are treated analytically in Refs. [21, 22] while Ref. [23] discusses the remaining errors in further detail. The errors comprise

1. Finite cyclicity [21]. With probability $1/(1 + C)$ the $|\uparrow\uparrow\downarrow\rangle$ trion wrongly decays "diagonally" to $|\downarrow\rangle$. The emitted photon is rejected by the etalon filters and is not detected. However, a diagonal decay during the early excitation may result in the emission and detection of a late photon resulting in dephasing of the quantum state.
2. Finite photon indistinguishability [21]. The scattering of a phonon during photon emission provides which-path information and dephases the quantum state.
3. Excitation errors [21]. Due to the finite detuning Δ_0 and pulse duration T_{opt} , the $|\downarrow\uparrow\downarrow\rangle$ trion may be excited and emit a photon. The photon is rejected by the etalons but provides which-path information and thus dephasing. Multi-photon emission also results in dephasing.

4. Spin rotation errors. As discussed in section 6.1, T_2^* and spin-flips with rate κ result in limited rotation fidelity. The two dampening mechanisms are implemented separately.
5. Spin initialization. Following the initialization pulse, the spin is the mixture $\hat{\rho} = F_i |\uparrow\rangle\langle\uparrow| + (1 - F_i) |\downarrow\rangle\langle\downarrow|$.
6. Spin readout. Given a photon detection during spin readout, the spin state is $|\uparrow\rangle$ with probability F_r . F_r is limited by laser background and imperfect dynamics, e.g. spin-flips and optical repumping coupling $|\uparrow\rangle$ and $|\downarrow\rangle$.
7. Finite classical interferometer visibility \mathcal{V}_{TBI} leads to reduced visibility in XX and YY basis.
8. Uncorrelated counts during the photonic detection windows (discussed in section 8.1).

Additionally, we model the optical loss of the system and use post-selection criteria identical to the experiment. Similar to the experiment, the simulated post-selection does not allow us to distinguish between photons emitted during or after an optical π -pulse. However, we assume that photons emitted during a π -pulse suffer an additional 6 dB loss based on their increased bandwidth and the narrowband etalon filters. This slightly increases fidelity, as "bad" trajectories with a photon emitted mid- π -pulse are less likely to pass post-selection.

Table S5 lists the contribution of each error and highlights spin rotations as the dominant error source. Additionally, spin initialization and readout can benefit from improvement but are less critical as their impact remains constant when increasing the number of photons.

A simulation including all error mechanisms yields $\mathcal{F}_{Bell}^{sim} = 67.8\%$ and the detection pattern in Fig. 2 of the main text. This is in good agreement with the measured raw fidelity $\mathcal{F}_{Bell}^{raw} = (65.7 \pm 0.4)\%$. Note that the infidelity $1 - \mathcal{F}_{Bell}^{sim}$ is less than the sum of infidelities in Table S5 as some errors will cancel out.

Error	\hat{P}_z	$\hat{\chi}$	Parameter value	Infidelity
Cyclicity	No (for Bell state)	Yes	$C = 14.7$	1.62% (simulated)
Phonon dephasing	No	Yes	$\mathcal{V}_{hom}^{corr} = 95.7\%$	2.34% (simulated)
Excitation	No (for $C \gg 1$)	Yes	$\gamma_0 = 2.54 \text{ ns}^{-1}$, $\Delta_0 = 17 \times 2\pi$, $T_{opt} = 35 \text{ ps}$.	2.66% (simulated)
Spin control (κ & T_2^*)	Yes	Yes	$T_2^* = 23.2 \text{ ns}$, $\kappa = 0.021 \text{ ns}^{-1}$	22.8% (simulated)
Spin readout	Yes	Yes	$F_r = 96.6\%$	5.1% (simulated)
Spin initialization	No	Yes	$F_i = 98\%$	2.0% (simulated)
Laser background, uncorrelated counts	Yes	Yes	Background estimates	2% (calculated)
Interferometer	No	Yes	$\mathcal{V}_{TBI} = 99.7\%$	0.15% (calculated)

Table S5: Summary of all considered error mechanism, their key parameter values, and their impact on Bell state fidelity (in absence of other errors) according to MC simulations using 10^6 trajectories and calculations. The \hat{P}_z and $\hat{\chi}$ columns indicate whether an error reduces visibility of ZZ and XX/YY-basis measurements, respectively.

10 Three-Qubit GHZ Measurement

As a proof of concept, we expand the experimental pulse sequence to emit a second time-bin entangled photon. Our target state is thus the three-qubit GHZ state

$$|\psi_{GHZ}\rangle = \frac{1}{\sqrt{2}} (|\uparrow, l_1, l_2\rangle + |\downarrow, e_1, e_2\rangle), \quad (29)$$

where $e(l)$ denotes an early(late) photon and the subscripts denote photons in the order of emission. Fig. S11 shows the full pulse sequence and a recorded histogram. As our setup only includes two detectors we are forced to add an 82.6 ns delay between the generation of the first and second photon to exceed the detector dead time. This extra delay could be removed by using detectors with faster recovery or detector multiplexing. Our post-selection is similar to the two-qubit case: We require at least one detection per photonic qubit and at least one detection from the spin readout. Using this requirement, our coincidence rate drops to 0.68 Hz.

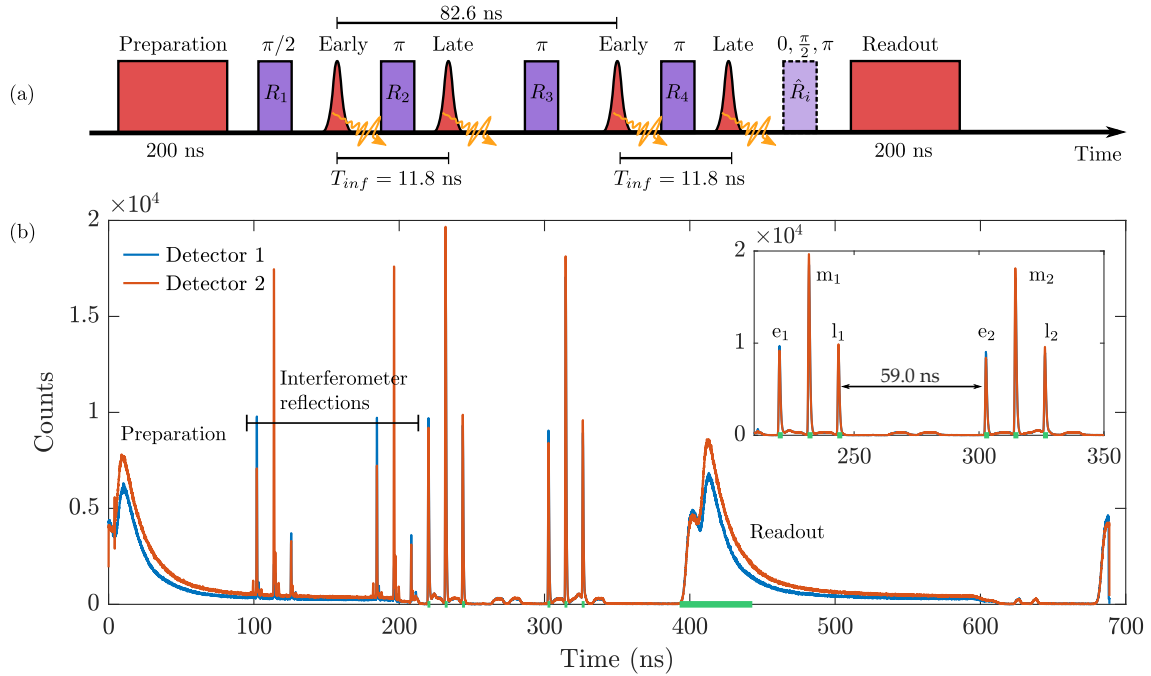


Figure S11: Three-qubit experiment. (a) Experimental pulse sequence. Two extra spin rotations (R_3 and R_4) and a second set of early/late optical excitations are added to generate a second time-bin encoded photon. (b) Histogram obtained from 300 seconds of acquisition. The green lines show detection windows. The inset shows a magnified view of the early(e), middle(m) and late(l) detection windows of the two photonic qubits.

Fig. S12a shows the raw histogram for the ZZZ -basis measurement and reveals a detection pattern with $\langle \hat{P}_z \rangle = (75.5 \pm 1.6)$. As expected, this visibility is lower than the two-qubit case as more operations (and especially Raman pulses) are performed.

Estimating $\hat{\chi}$ now requires measuring the operators [18]

$$\hat{\mathcal{M}}_k = \left[\cos\left(\frac{k\pi}{N}\right) \hat{\sigma}_x + \sin\left(\frac{k\pi}{N}\right) \hat{\sigma}_y \right]^{\otimes N}, \quad \text{for } k = \{1, 2, 3\}. \quad (30)$$

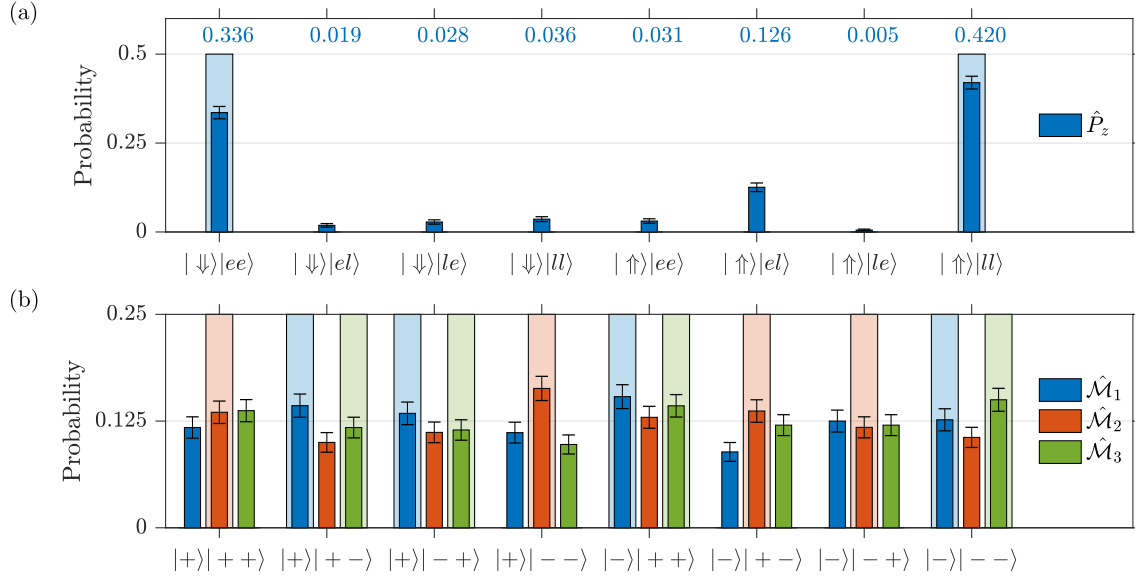


Figure S12: Fidelity estimation of a three-qubit GHZ state. Probabilities are normalized across all outcomes. Shaded bars represent ideal outcomes. Errorbars are derived from shot noise. **(a)** Measurements in ZZZ-basis. **(b)** Measurements of three equidistant projectors on the Bloch sphere equator. Each state on the x-axis is an eigenstate of $\hat{\mathcal{M}}_i$. The qubits are in the order of spin, photon 1 and photon 2.

The raw measurement outcomes are given in Fig. S12b and give rise to the visibilities in Table S6. We note that $\langle \hat{\chi} \rangle$ is larger than zero by more than three standard deviations and thus represents a significant coherence. However, we do not exceed the $\mathcal{F} = 0.5$ threshold for entanglement.

	Ideal value	Estimated value
$\langle \hat{P}_z \rangle$	1	0.755 ± 0.016
$\langle \hat{\mathcal{M}}_1 \rangle$	-1	-0.11 ± 0.04
$\langle \hat{\mathcal{M}}_2 \rangle$	+1	0.11 ± 0.04
$\langle \hat{\mathcal{M}}_3 \rangle$	-1	-0.05 ± 0.04
$\langle \hat{\chi} \rangle = \frac{1}{3} \sum_{k=1}^3 (-1)^k \hat{\mathcal{M}}_k$	1	0.09 ± 0.02
$\mathcal{F}_{GHZ}^{N=3} = \frac{\langle \hat{P}_z \rangle + \langle \hat{\chi} \rangle}{2}$	100%	$(42.3 \pm 1.4)\%$

Table S6: Fidelity estimates using raw measurements of a three-qubit GHZ state.

11 Effect of Spectral Diffusion and Blinking

Spectral diffusion and blinking are observed in the studied quantum dot, yet we exclude these effects from our analysis for the following reasons:

1. Spectral diffusion mainly affects the fidelity of spin initialization and readout by randomly detuning the cycling transition from the pumping laser. The optical π -pulse is largely unaffected as the diffusion magnitude $\sigma/2\pi \approx 345$ MHz [1] is small compared to the π -pulse bandwidth $\approx 0.44/T_{opt} \approx 13$ GHz where 0.44 is the Gaussian time-bandwidth product.
2. Due to the long ms-timescale of spectral diffusion [24], subsequently emitted photons will remain indistinguishable as explicitly demonstrated in recent experiments [2]. Reducing spectral diffusion is however important for fusing cluster states generated by separate QDs.
3. Blinking reduces the protocol success probability but does not appreciably reduce the entanglement fidelity due to our post-selection criteria. If (as we expect) the blinking is due to a probabilistic hole initialization at the cycle onset, it only results in a linear decrease in success probability.
4. Finally, recent experiments continue to show improvements to blinking and spectral diffusion. Here we highlight the observation of a virtually blinking-free QD embedded in a PCW [2] and the interference of identical photons from independent QDs with <10% inhomogeneous broadening [25].

References

- [1] M. H. Appel, A. Tiranov, A. Javadi, M. C. Löbl, Y. Wang, S. Scholz, A. D. Wieck, A. Ludwig, R. J. Warburton, and P. Lodahl, *Phys. Rev. Lett.* **126**, 013602 (2021).
- [2] R. Uppu, F. T. Pedersen, Y. Wang, C. T. Olesen, C. Papon, X. Zhou, L. Midolo, S. Scholz, A. D. Wieck, A. Ludwig, and P. Lodahl, *Sci. Adv.* **6**, eabc8268 (2020).
- [3] J. H. Bodey, R. Stockill, E. V. Denning, D. A. Gangloff, G. Éthier-Majcher, D. M. Jackson, E. Clarke, M. Hugues, C. L. Gall, and M. Atatüre, *npj Quantum Inf.* **5**, 95 (2019).
- [4] E. Hecht, *Optics*, 4th ed. (Addison Wesley, 2002).
- [5] X. Zhou, I. Kulkova, T. Lund-Hansen, S. L. Hansen, P. Lodahl, and L. Midolo, *Appl. Phys. Lett.* **113**, 251103 (2018).
- [6] P. Lodahl, S. Mahmoodian, and S. Stobbe, *Rev. Mod. Phys.* **87**, 347 (2015).
- [7] C. Gerry and P. Knight, *Introductory Quantum Optics*, 1st ed. (Cambridge University Press, 2005).
- [8] B. Urbaszek, X. Marie, T. Amand, O. Krebs, P. Voisin, P. Maletinsky, A. Högele, and A. Imamoglu, *Rev. Mod. Phys.* **85**, 79 (2013).
- [9] L. Huthmacher, R. Stockill, E. Clarke, M. Hugues, C. LeGall, and M. Atatüre, *Phys. Rev. B* **97**, 241413(R) (2018).
- [10] J. H. Prechtel, A. V. Kuhlmann, J. Houel, A. Ludwig, S. R. Valentin, A. D. Wieck, and R. J. Warburton, *Nat. Mater.* **15**, 981 (2016).
- [11] T. M. Godden, J. H. Quilter, A. J. Ramsay, Y. Wu, P. Brereton, S. J. Boyle, I. J. Luxmoore, J. Puebla-Nunez, A. M. Fox, and M. S. Skolnick, *Phys. Rev. Lett.* **108**, 017402 (2012).
- [12] A. Delteil, Z. Sun, W.-b. Gao, E. Togan, S. Faelt, and A. Imamoglu, *Nature Physics* **12**, 218 (2016).
- [13] D. Ding, M. H. Appel, A. Javadi, X. Zhou, M. C. Löbl, I. Söllner, R. Schott, C. Papon, T. Pregolato, L. Midolo, A. D. Wieck, A. Ludwig, R. J. Warburton, T. Schröder, and P. Lodahl, *Phys. Rev. Appl.* **11**, 031002 (2019).
- [14] C. K. Hong, Z. Y. Ou, and L. Mandel, *Phys. Rev. Lett.* **59**, 2044 (1987).
- [15] C. Santori, D. Fattal, J. Vučković, G. S. Solomon, and Y. Yamamoto, *Nature* **419**, 594 (2002).
- [16] H. Ollivier, S. E. Thomas, S. C. Wein, I. Maillette de Buy Wenniger, N. Coste, J. C. Loredó, N. Somaschi, A. Harouri, A. Lemaitre, I. Sagnes, L. Lanco, C. Simon, C. Anton, O. Krebs, and P. Senellart, *Phys. Rev. Lett.* **126**, 063602 (2021).
- [17] P. Tighineanu, C. L. Dreeßen, C. Flindt, P. Lodahl, and A. S. Sørensen, *Phys. Rev. Lett.* **120**, 257401 (2018).
- [18] O. Gühne, C. Y. Lu, W. B. Gao, and J. W. Pan, *Phys. Rev. A* **76**, 030305(R) (2007).
- [19] C. W. Chou, H. de Riedmatten, D. Felinto, S. V. Polyakov, S. J. van Enk, and H. J. Kimble, *Nature* **438**, 828 (2005), number: 7069 Publisher: Nature Publishing Group.

- [20] O. Gühne and G. Tóth, [Physics Reports](#) **474**, 1 (2009), publisher: Elsevier B.V.
- [21] K. Tiurev, P. L. Mirambell, M. B. Lauritzen, M. H. Appel, A. Tiranov, P. Lodahl, and A. S. Sørensen, [Phys. Rev. A](#) **104**, 052604 (2021).
- [22] K. Tiurev, M. H. Appel, P. L. Mirambell, M. B. Lauritzen, A. Tiranov, P. Lodahl, and A. S. Sørensen, [Phys. Rev. A](#) **105**, L030601 (2022).
- [23] M. H. Appel, *A Quantum Dot Source of Time-Bin Multi-Photon Entanglement*, [Phd thesis](#), University of Copenhagen (2021).
- [24] A. V. Kuhlmann, J. Houel, A. Ludwig, L. Greuter, D. Reuter, A. D. Wieck, M. Poggio, and R. J. Warburton, [Nature Physics](#) **9**, 570 (2013), publisher: Nature Publishing Group.
- [25] L. Zhai, G. N. Nguyen, C. Spinnler, J. Ritzmann, M. C. Löbl, A. D. Wieck, A. Ludwig, A. Javadi, and R. J. Warburton, [arXiv:2106.03871](#) (2021).